Full-Permutation Dynamical Decoupling in Triple-Quantum-Dot Spin Qubits

Bo Sun,* Teresa Brecht, Bryan H. Fong, Moonmoon Akmal, Jacob Z. Blumoff, Tyler A. Cain, Faustin W. Carter, Dylan H. Finestone, Micha N. Fireman, Wonill Ha, Anthony T. Hatke, Ryan M. Hickey, Clayton A. C. Jackson, Ian Jenkins, Aaron M. Jones, Andrew Pan, Daniel R. Ward, Aaron J. Weinstein, Samuel J. Whiteley, Parker Williams, Matthew G. Borselli, Matthew T. Rakher, and Thaddeus D. Ladd

HRL Laboratories, LLC, 3011 Malibu Canyon Road, Malibu, California 90265 USA

(Received 9 September 2022; revised 22 February 2024; accepted 17 April 2024; published 11 June 2024)

Dynamical decoupling of spin qubits in silicon can increase fidelity and can be used to extract the frequency spectra of noise processes. We demonstrate a full-permutation dynamical decoupling technique that cyclically exchanges the spins in a triple-quantum-dot qubit. This sequence not only suppresses both low-frequency charge-noise-induced and magnetic-noise-induced errors; it also refocuses leakage errors to first order, which is particularly interesting for encoded exchange-only qubits. For a specific construction, which we call "NZ1y," the qubit is isolated from error sources to such a degree that we measure a remarkable exchange pulse error of 2.8×10^{-5}. This sequence maintains a quantum state for roughly 18,000 exchange pulses, extending the qubit coherence from $T_2^* = 2$ μs to $T_2 = 720$ μs. We experimentally validate an error model that includes $1/f$ charge noise and $1/f$ magnetic noise in two ways: by direct exchange-qubit simulation and by integration of the assumed noise spectra with derived filter functions, both of which reproduce the measured error and leakage with respect to a change of the repetition rate.

DOI: 10.1103/PRXQuantum.5.020356

I. INTRODUCTION

Dynamical decoupling (DD) sequences suppress dephasing in quantum systems by periodically inverting interactions between the qubit and its environment [1,2]. Applied to qubits based on electron spins in silicon, DD can extend qubit coherence times to more than 1 s in donor-bound spins [3] and to more than 20 ms in quantum dots [4]. For nuclei in silicon, dynamically decoupled coherence times have been shown to be at least hours long for ensembles [5] and more than 30 s for a single nucleus [6]. While extended qubit memory is one motivation for DD experiments, the present work focuses on another key function: DD can expose features of noise processes relevant to qubit performance in quantum information processing systems. Specifically, periodic DD sequences act as frequency-domain filters applied to the noise spectrum witnessed by spins. By using this filter-function formalism, one can invert time-domain DD data to extract frequency-domain noise spectra [7–14].

*Corresponding author: bsun@hrl.com

A standard DD process is the Hahn spin echo [15], in which the effective interaction between a spin and its local magnetic field is periodically reversed by application of spin-flipping π pulses. In this work, we demonstrate a somewhat different application in our system, beginning by preparing three spins as a decoherence-free subsystem (DFS), for which the total spin projection is a degree of freedom that is removed from initialization, control, and readout [16–18]. The DFS is insensitive to global fields that couple to the total spin projection, but is sensitive to local sources of noise: magnetic field gradients and charge noise. Our decoupling sequence then relies on the principle of periodically and symmetrically permuting the three spins, which causes local noise to average into a global term to which the encoded DFS is impervious [19,20]. We refer to this process as "full-permutation dynamical decoupling." Unlike electron shuttling techniques [21], this form of DD exchanges only the electron spin state, and it is particularly well suited to exchange-only qubits as the DFS subspace also serves as a basis for encoded universal control using the voltage-controlled exchange interaction [17,18,22–26]. In this paper, we demonstrate that full-permutation DD can suppress error rates to 2.8×10^{-5} per control pulse, which is a reduction by a factor of almost 50 compared with the error rate of the same qubit obtained from randomized benchmarking (1.3×10^{-3} per exchange pulse). Furthermore, we show that this decoupling sequence can be used to verify our understanding of qubit noise sources by comparing experimental results with simulation across regimes of magnetic noise and charge noise dominance, accessed by our varying the repetition rate. We show that the sequence we use is robust with regard to low-frequency noise as well as miscalibration, and it therefore allows us to validate a $1/f$ spectral character of each of these noise sources to greater precision than is possible with methods such as randomized benchmarking, which elucidates design trade-offs for future device iterations.

We begin by describing our triple-quantum-dot qubit in Sec. II. We then detail the structure and noise-filtering capability of full-permutation DD in Sec. III, followed by the experimental results in Sec. IV. As we discuss, this decoupling strategy is highly effective at eliminating dephasing due to local magnetic fields that vary slowly compared with the timescale of the qubit control pulses. This provides a key gauge of operational noise for the DFS system.

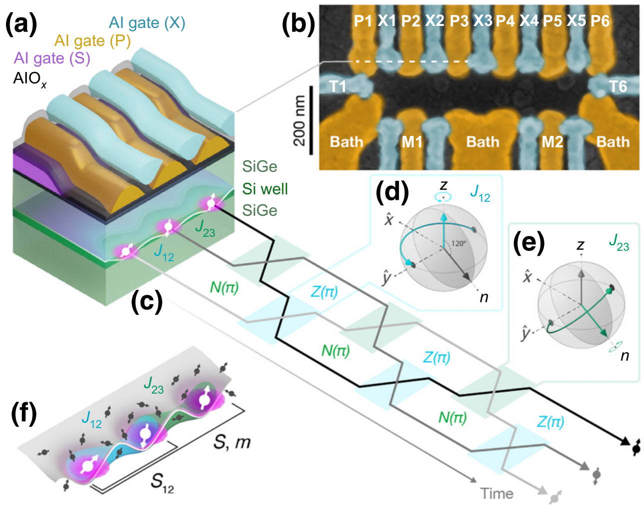

FIG. 1. Full-permutation DD (NZ1 sequence) in an exchange-only triple-quantum-dot qubit. (a) Three-dimensional sketch of the Si/SiGe heterostructure and gate stack, including three electron spins occupying quantum dots in the quantum well confined laterally by the gate stack above. (b) False-color scanning electron micrograph with plunger gates (P), exchange gates (X), bath-tunnel-barrier gates (T), and electrometer gates (M) labeled. (c) The decoupling sequence. (d) Bloch sphere showing π rotation on J_{12} (or Z operation) resulting from a pulse on the X1 gate. (e) Bloch sphere showing π rotation on J_{23} (or N operation) resulting from a pulse on the X2 gate. (f) Illustration showing randomly oriented spinful nuclei of the lattice (gray arrows), the slow fluctuations of which may be dynamically decoupled.

II. THE Si/SiGe EXCHANGE-ONLY TRIPLE-QUANTUM-DOT QUBIT

A. Device description

In this paper, we explore the performance of a full-permutation DD sequence applied to an exchange-only triple-quantum-dot qubit within an isotopically enhanced silicon quantum well [24,25,27,28]. The quantum dots are formed by the electrostatic potential created by patterned metal gates on a SiGe/^{28}Si/SiGe heterostructure, in which the quantum well is 3 nm thick and the ^{29}Si content is reduced to 800 ppm. In contrast to recent devices fabricated by the single-layer etch-defined gate electrode (SLEDGE) technique [29], this device uses an Al overlapping gate design [25,27,30]. A false-color scanning electron micrograph of a representative device is shown in Fig. 1(b), where the plunger gate (P) voltages are adjusted to trap a single electron, and the exchange interaction between neighboring electrons is controlled by voltages applied to the exchange gates (X). Readout is achieved with use of charge sensors (M) and a signal chain described in Ref. [31]. The device geometry and methods of calibration and control are the same as in Ref. [18].

In this device, we focus on gates P1, P2, and P3, each of which traps a single spin. The eight basis states for these three spins may be written as $|S_{12}, S; m\rangle$, where $S = 1/2, 3/2$ is the total spin quantum number across all three quantum dots, corresponding to $\mathbf{S} = \mathbf{S}_1 + \mathbf{S}_2 + \mathbf{S}_3$, $m = -S, 1-S, \ldots, S$ is the total spin projection, and S_{12} is the combined spin of the electrons in quantum dots 1 and 2, corresponding to $\mathbf{S}_{12} = \mathbf{S}_1 + \mathbf{S}_2$. This assignment of spin quantum numbers is shown in cartoon form in Fig. 1(f) and discussed in Ref. [32]. The encoded DFS qubit lives in the subsystem where $S = 1/2$. Encoded $|0\rangle = |0, 1/2; m\rangle$ is the singlet state of the first two spins, and encoded $|1\rangle = |1, 1/2; m\rangle$ is a superposition of the triplet states of the first two spins; both of these "states" are doublets for $m = \pm 1/2$. A random selection of the two $|0\rangle$ states is initialized by our preparing the first two spins in a singlet ground state, leaving the third spin unpolarized [24], i.e., $\rho_0 = \sum_{m=\pm 1/2} |0, 1/2; m\rangle\langle 0, 1/2; m| \,/2$. The S_{12} quantum number is directly read out via singlet-triplet readout using Pauli spin blockade, which provides no information about S or m. The four states $|1, 3/2; m\rangle$ (which we refer to collectively as "$|Q\rangle$," for "quadruplet"), are outside the DFS and are referred to as "leaked states." Since all $|Q\rangle$ states have $S_{12} = 1$, they appear as encoded $|1\rangle$ during measurement.

This qubit is universally controllable via exchange interactions alone [17,18,22,32], i.e., with the control Hamiltonian

$$H_{\text{control}}(t) = J_{12}(t)\mathbf{S}_1 \cdot \mathbf{S}_2 + J_{23}(t)\mathbf{S}_2 \cdot \mathbf{S}_3, \qquad (1)$$

where $\mathbf{S}_j$ is the single-spin operator for spin j and $J_{jk}(t)$ is the time-varying exchange energy between spins j and k. Each exchange interaction is activated by our pulsing the voltage of an X gate above a tunnel barrier between quantum dots; enhanced tunneling reduces the energy of the singlet state between those two spins for the duration of the pulse. The symmetry of this exchange-only Hamiltonian means it has no impact on quantum numbers S or m; it impacts only the S_{12} quantum number. For the single qubit we study here, we may therefore provide a geometric analogy for exchange gates. In the Bloch-sphere representation of the DFS, Figs. 1(d) and 1(e), exchange between quantum dots 1 and 2 drives rotations about the z-axis, and exchange between quantum dots 2 and 3 drives rotations about the n-axis, which is 120° separated from z in the x-z plane (according to Clebsch-Gordan coefficients.) Full control is therefore possible with use of calibrated exchange pulses on these axes. For full-permutation DD, the only calibrated exchange pulse needed is the π pulse, which enacts a full spin swap. A π pulse about the z-axis, abbreviated Z, is a swap of spins 1 and 2. A π pulse about the n-axis, abbreviated N, is a swap of spins 2 and 3.

B. Noise description

Here we classify noise in our system as coming from one of two forms. The first is magnetic field noise, described by the Hamiltonian

$$H_B = -g\mu_B \sum_j \mathbf{B}_j(t) \cdot \mathbf{S}_j + \sum_{jk} A_{jk}\mathbf{I}_k \cdot \mathbf{S}_j, \quad (2)$$

where g is the gyromagnetic ratio (approximately 2 in Si), μ_B is the Bohr magneton, $\mathbf{B}_j$ is the magnetic field at quantum dot j, $\mathbf{I}_k$ is the spin of the kth nuclear spin (^{29}Si or ^{73}Ge) in the Si/SiGe heterostructure, and A_{jk} is the contact hyperfine coupling energy, which is proportional to the probability of finding spin j at the location of nucleus k [9]. For simplicity, we define an effective-field angular frequency $\mathbf{b}_j = (-g\mu_B\mathbf{B}_j + \sum_k A_{jk}\mathbf{I}_k)/\hbar$, so $H_B = \hbar\sum_j \mathbf{b}_j \cdot \mathbf{S}_j$.

Our DFS encoding ensures that neither a static value nor random fluctuations in $\sum_j \mathbf{b}_j(t)$ have any measurable effect on our qubit, since global fluctuating magnetic fields couple to only the $\mathbf{S}$ degree of freedom, which impacts only m, but not our qubit degree of freedom S_{12}. However, gradients such as $\mathbf{b}_1 - \mathbf{b}_2$ do not conserve the S_{12}, S, and m quantum numbers, and thus cause decoherence by both impacting subsystem qubit states and causing leakage out of the DFS.

The noise vectors $\mathbf{b}_j(t)$ have both static and dynamic microscopic contributions. Static contributions to $\mathbf{b}_j$ arise, especially at high applied magnetic field, from magnetic field gradients originating from screening of any applied magnetic field and from spin-orbit effects, as discussed in Ref. [9]. In the present case, these static noise terms are negligible, both because we apply no significant field (only Earth's field is present) and because static fields are well decoupled by our permutational dynamical decoupling procedure, as we discuss. The most important contributions to gradients in $\mathbf{b}_j$ are dynamic, resulting from the spatially random fluctuating ^{29}Si and ^{73}Ge nuclear spins present in our devices. The dynamics of the nuclear spin vector in a quantum dot, $\langle \mathbf{I}_k(t)\rangle$, are governed by nuclear dipole-dipole interactions, by the nutations resulting from the interplay of Zeeman and quadrupolar internal dynamics for ^{73}Ge nuclei [9] and by the nuclei's contact hyperfine interactions with electrons. A detailed quantum treatment of this bath including nuclear-nuclear entanglement as well as entanglement to electron spins is a deeply challenging theoretical problem, but we find that, at least for the timescales of the present experiments, these dynamics may be treated as a classical Gaussian noise source characterized by noise power spectral density (PSD) $S_B(\nu)$. Prior direct measurements of singlet-triplet oscillation frequency fluctuations [24] or double-quantum-dot exchange echo noise spectroscopy [9] in samples highly similar to the present device has indicated that $S_B(\nu)$ has a strongly $1/f$ character, with two notable exceptions. At high field, measured $1/f^{\alpha}$ spectra take on values of α greater than 1; the present experiments do not access these field regimes. At very low fields, the transverse (or flip-flop) terms of the contact hyperfine interaction [the part of Eq. (2) expressed as spin-raising and spin-lowering operators as $I_k^+S_j^- + I_k^-S_j^-$] may be roughly understood as oscillating at the sum or difference of the electron Larmor frequency ($g\mu_B/h$) and the nuclear Larmor frequency (which is small enough to ignore). In a classical-bath description of the nuclear noise, this introduces sidebands of an otherwise single-lobed $1/f$ spectrum $S_B(\nu)$ at $S_B(\nu \pm g\mu_B/h)$; the detail of this effect is connected with the definition of a noise filter function, which we discuss in the next section and elaborate in Appendix A. In the present work, we rely on these prior measurements of the *shape* of the noise spectrum, as well as direct calibrations of its *amplitude*, to hypothesize a classical magnetic noise spectrum $S_B(\nu)$ of $1/f$ shape with Larmor sidelobes and validate this noise model against direct decoupling measurements.

A second form of relevant noise besides magnetic sources comes from imperfect exchange operations. When we apply a π pulse of duration t_{pulse} on spins 2 and 3, the integrated angle is

$$\frac{1}{\hbar}\int_t^{t+t_{\text{pulse}}} (J_{23}(\tau) + \delta J_{23}(\tau))d\tau = \pi + \delta\theta_n(t), \quad (3)$$

where the noise $\delta J_{23}(t)$ may result from various sources, including miscalibration, local charge noise, and noise from control instruments. As a result, when we attempt to perfectly swap spins 2 and 3, we deviate from this ideal by $\exp(-i\delta\theta_n\mathbf{S}_2 \cdot \mathbf{S}_3)$, which is interpretable as over-rotation or under-rotation about the n-axis. Likewise, noise on $J_{12}(t)$ causes an integrated angle deviation of $\delta\theta_z(t)$. Such deviations cause qubit error, but they conserve S and m and consequently do not cause leakage.

As for magnetic noise, significant prior work on the direct low-frequency measurement of exchange noise $\delta J_{jk}(t)$ has been performed by us [24,25] and others [14] and indicates that this noise may be well described as classical Gaussian noise with a strongly $1/f$ spectrum $S_E(\nu)$ (the PSD of $\delta J_{jk}(t)/\hbar$) over many decades of frequency ν. As with magnetic noise, we rely on these prior measurements of the *shape* of the noise spectrum, as well as direct calibrations of its *amplitude*, to hypothesize a classical electric noise spectrum $S_E(\nu)$ of $1/f$ shape and we validate this noise model against direct decoupling measurements, the nature of which we now detail.

III. FULL-PERMUTATION DYNAMICAL DECOUPLING

A. Average Hamiltonian description

The theory of full-permutation DD was established in Ref. [19], and was elaborated in Ref. [20] to include the development of sequences of higher order than we apply here. Full-permutation DD homogenizes the gradient magnetic field across the three spins by successively swapping pairs of spins in the triple-quantum-dot qubit. In the Bloch-sphere picture for the exchange-only qubit, the sequence applies alternating rotations around the n-axis and the z-axis, and hence we use a shorthand to refer to full-permutation DD as an “NZ” sequence. The NZ sequence is illustrated by the braid in Fig. 1(c), which shows that over the duration of three repetitions of NZ, each spin spends an equal amount of time localized within each quantum dot before returning to its initial position. Thus, the six-pulse sequence NZNZNZ forms the base decoupling block. As this is a first-order sequence relative to the constructions in Ref. [20], we refer to it as “NZ1.”

Analogously to the analysis of the Carr-Purcell-Meiboom-Gill sequence developed half a century ago in the context of nuclear magnetic resonance [33,34], the operation of the NZ1 sequence on qubit states in the presence of low-frequency noise and static inhomogeneities may be understood via average Hamiltonian theory. For this, we consider our total noise Hamiltonian discussed in Sec. II,

$$H_{\text{noise}}(t) = \sum_j \hbar \mathbf{b}_j(t)\cdot\mathbf{S}_j + \delta J_{12}(t)\mathbf{S}_1\cdot\mathbf{S}_2 + \delta J_{23}(t)\mathbf{S}_2\cdot\mathbf{S}_3, \tag{4}$$

modulated by the “toggling frame” or interaction picture:

$$\tilde{H}_{\text{noise}}(t) = U^\dagger_{\text{NZ1}}(t) H_{\text{noise}}(t) U_{\text{NZ1}}(t). \tag{5}$$

Here $U_{\text{NZ1}}(t)$ is the periodic unitary corresponding to application of exchange swaps, alternating between N and Z square pulses of duration t_{pulse} interspersed by periods of duration t_{idle}, where exchange is negligible. This unitary is straightforward to calculate for any exchange pulse shape $J_{jk}(t)$, as long as the pulses for $J_{12}(t)$ and $J_{23}(t)$ never overlap in time. If the time dependence of Eq. (4) is either very slow relative to the period of $U_{\text{NZ1}}(t)$ or has the same periodicity (as in the $\delta J_{jk}(t)$ terms), then Floquet’s theorem ensures that $\tilde{H}_{\text{noise}}(t)$ generates a unitary of the form $U_p(t)\exp(-iFt)$, where $U_p(t)$ has the same periodicity as $U_{\text{NZ1}}(t)$, so $U_p(MT) = 1$ for an integer M number of repeated sequences each performed with period time T. F is the Floquet Hamiltonian, which, if measured at each full period of six pulses, captures the slow dynamics of the spins due to H_{noise}.

F may be calculated perturbatively with use of the Magnus expansion over a full period of $U_{\text{NZ1}}(t)$ as $F = \sum_n \bar{H}^{(n)}$, with each term nth order in H_{noise}. For the present analysis of NZ1, we consider only the lowest-order term:

$$\bar{H}^{(0)} = \frac{1}{T}\int_0^T d\tau \tilde{H}_{\text{noise}}(\tau). \tag{6}$$

The result of this calculation (with period $T = 6t_{\text{pulse}} + 6t_{\text{idle}}$) is

$$\begin{aligned}\frac{1}{\hbar}\bar{H}^{(0)} = {} & \frac{\delta\theta_n + \delta\theta_z}{16t_{\text{pulse}} + 16t_{\text{idle}}}(-1)^{S-1/2} + \frac{\mathbf{b}_1+\mathbf{b}_2+\mathbf{b}_3}{3}\cdot\mathbf{S} \\ & + \frac{t_{\text{pulse}}}{12t_{\text{pulse}}+12t_{\text{idle}}}\{[(\mathbf{b}_2-\mathbf{b}_3)C_{23} + (\mathbf{b}_2-\mathbf{b}_1)C_{12}] \\ & \cdot[\mathbf{S}_1\times\mathbf{S}_2 + \mathbf{S}_2\times\mathbf{S}_3 + \mathbf{S}_3\times\mathbf{S}_1]\},\end{aligned} \tag{7}$$

where

$$C_{jk} = \frac{1}{2t_{\text{pulse}}}\int_0^{t_{\text{pulse}}} \sin\left(\frac{1}{\hbar}\int_0^t J_{jk}(t')dt'\right)dt. \tag{8}$$

From this expression, the exchange noise terms (i.e., containing $\delta\theta_\alpha$) provide only a phase shift to leakage spaces, and the average magnetic field $\sum_k \mathbf{b}_k/3$ couples only to $\mathbf{S}$, which impacts only m. Notably, neither of these effects is detectable or impactful on the encoded qubit. The remaining terms depend on magnetic gradients $\mathbf{b}_j - \mathbf{b}_k$ and finite pulse widths. To see the impact of these terms, we find that

$$\begin{aligned}&\mathbf{S}_1\times\mathbf{S}_2 + \mathbf{S}_2\times\mathbf{S}_3 + \mathbf{S}_3\times\mathbf{S}_1 \\ &\quad = 4(\mathbf{S}_1\times\mathbf{S}_2\cdot\mathbf{S}_3)\mathbf{S} = \sqrt{3}\sigma^y\mathbf{S},\end{aligned}$$

where σ^y is the Pauli y operator on the S_{12} degree of freedom of the encoded qubit [32]. Again $\mathbf{S}$ impacts only m, and so this remaining term is proportional strictly to σ^y in the encoded subspace and, remarkably, does not cause leakage. Hence, if we ignore gauge and overall phase, effectively

$$\bar{H}^{(0)} \propto \sigma^y. \tag{9}$$

When one is initializing $|0\rangle$, the σ^y dependence results in oscillations of the final singlet return probability with frequency proportional to t_{pulse} and to field gradients, which, due to nuclear dynamics, undergo slow fluctuations, resulting in an apparent decay. These oscillations could be refocused with use of higher-order sequences such as the NZ2 sequence NZNZNZZNZNZN [20]. Here we use an alternative method, similar to the reduction of static pulsing errors in Ref. [34]: we choose to prepare our qubit along the y-axis of the Bloch sphere such that $\bar{H}^{(0)}$ causes no evolution except on the ignored m degree of freedom. We do this by including composite single-DFS-qubit rotations so that the evolution becomes, ignoring gauge and overall phase, effectively

$$U(MT) \approx \mathbb{H}\mathbb{S}^\dagger e^{-i\bar{H}^{(0)}MT/\hbar}\mathbb{S}\mathbb{H} \propto e^{-i\sigma^z\omega_b' nT}, \tag{10}$$

where ω_b' is some frequency resulting from the third term of Eq. (7), $\mathbb{S} = \text{diag}(1, i)$ in the qubit basis, and $\mathbb{H}$ is the Hadamard gate (see Ref. [18] for calibration and construction of these single-qubit gates). This operator is effectively identity on the prepared and measured singlet $|0, S_{12}; m\rangle$ state, regardless of any first-order static field gradient or exchange angle offset. Since this NZ sequence is first order and applied in the y basis, we refer to this construction as "NZ1y."

For the purposes of this paper and specifically the analysis of NZ1y sequences, we *define* the error of the NZ1y sequence as

$$\epsilon_{\text{NZ1y}} = \lim_{M\to\infty} \frac{1 - \langle |\langle y|\, U(MT)\, |y\rangle|^2\rangle}{M}; \tag{11}$$

that is, the probability of *not* returning to the $|y\rangle = \mathbb{S}\mathbb{H}\,|0\rangle$ state after M repetitions of NZ1 for an ensemble average (denoted $\langle\cdot\rangle$) of noisy unitary processes $U(MT)$, divided by M for large values of M. We likewise estimate the per-pulse error ϵ_{PP} as simply $\epsilon_{\text{NZ1y}}/6$, noting that relative to low-frequency noise, error cancellations occur only after full cycles of six pulses, leaving this definition of ϵ_{PP} physically meaningful if there were no time correlations in the noise to a pulse (i.e., white noise), and as strictly a convenient definition for highly-time-correlated noise. Likewise, for NZ1 without $|y\rangle$ preparation, which might be written NZ1z, we consider the error as the probability of not returning to the $|0\rangle$ state rather than the $|y\rangle$ state. We acknowledge that we are not performing full process tomography in the present work, and therefore these "errors" are not the result of full characterizations of quantum processes and cannot be rigorously taken as process infidelities. However, to make some approximate connection, we note that the error as defined here would be consistent with the "gate" or "process" infidelity if the process were a strictly depolarizing channel (although calculations give no expectations for it to be so).

The average Hamiltonian analysis thus far has considered the first-order term of F only, and has found that both static magnetic and exchange noise contributions to ϵ_{NZ1y} vanish entirely at this order. We may find the impact of static noise at higher orders by analyzing higher orders of the Magnus expansion. In doing so, for one repetition of NZ1, we find that static exchange error angles $\delta\theta_n$ and $\delta\theta_z$ contribute in the next order when initialization is performed along the z-axis (NZ1z), showing a coherent error of size $(3/64)(\delta\theta_n^2 + \delta\theta_z^2 - 4\delta\theta_z\delta\theta_n)^2$. For initialization along the y-axis (NZ1y), these errors are canceled even at second order, and to third order

Miscalibration contribution to $\epsilon_{\text{NZ1y}} \approx$

$$\frac{1}{64}(\delta\theta_n^2 + \delta\theta_z^2 - 4\delta\theta_z\delta\theta_n)^2(\delta\theta_n^2 + \delta\theta_z^2 - \delta\theta_z\delta\theta_n). \tag{12}$$

The resilience of NZ1y to static miscalibration error makes it especially effective at exposing noise at higher frequencies.

B. Filter function description

Average Hamiltonian theory has helped us understand and explain how NZ1 and NZ1y cancel static magnetic gradients and miscalibrations; however, it is not effective at handling noise that dynamically fluctuates during the sequence. For this, we instead use a filter function formalism, derived in Appendix A. With this, we find

$$\begin{aligned} 1 - \langle|\langle 0|U(t_{\text{pulse}}, t_{\text{idle}})|0\rangle|^2\rangle \approx \\ \int_0^\infty d\nu\, S_B(\nu)\mathcal{F}_{\mathcal{M}}^{\mathcal{I}}(\nu, t_{\text{pulse}}, t_{\text{idle}}) \\ + \int_0^\infty d\nu\, S_E(\nu)\mathcal{F}_E^{\mathcal{I}}(\nu, t_{\text{pulse}}, t_{\text{idle}}), \end{aligned} \tag{13}$$

where $S_B(\nu)$, the single-sided noise PSD for each vector component of $\mathbf{b}_j(t)$, is assumed independent and identical on each quantum dot and component, and $S_E(\nu)$ is likewise assumed to be independent and identical for each pair of quantum dots within an exchange axis. As usual for the filter function formalism, the magnetic and exchange filter functions for infidelity, $\mathcal{F}_{\mathcal{M}}^{\mathcal{I}}(\nu, t_{\text{pulse}}, t_{\text{idle}})$ and $\mathcal{F}_E^{\mathcal{I}}(\nu, t_{\text{pulse}}, t_{\text{idle}})$, respectively, are oscillatory, with a central peak dictated by the frequency of pulsing and with a passband that narrows with the number of pulses, and somewhat with the shape of the pulses (see Appendix B), although all calculations reported in the main text use a square-pulse approximation. Note that $\mathbf{b}_j(t)$ can describe noncollinear time-dependent noise, and that δJ_{jk} can vary from pulse to pulse. In this way, our derivation encapsulates quasistatic noise and white Johnson noise as well as $1/f$ noise.

Our calculation shows that for charge noise, the NZ1y filter function is given by

$$\mathcal{F}_E^{\mathcal{I}}(\nu, M, t_{\text{pulse}}, t_{\text{idle}}) = \frac{2(2+\cos 4\pi\nu\tau)\sin^2(\pi\nu t_{\text{pulse}})\sin^2(2\pi\nu\tau)}{\pi^2\nu^2} \times \frac{\sin^2(6M\pi\nu\tau)}{\sin^2(6\pi\nu\tau)}, \quad (14)$$

where $\tau = t_{\text{idle}} + t_{\text{pulse}}$ and M is the number of six-pulse NZNZNZ repetitions.

The filter function for $\mathcal{F}_{\mathcal{M}}^{\mathcal{I}}(\nu, M, t_{\text{pulse}}, t_{\text{idle}})$ is more complicated. This function has a "central peak" with replica sidebands at $\pm g\mu_B B_0/\hbar$, the electron Larmor frequency. The zero frequency ($\nu = 0$) limit of this central peak, for a general state initialized on the Bloch sphere determined by the polar coordinates θ and ϕ, is given by

$$\mathcal{F}_{\mathcal{M}}^{\mathcal{I}}(0, M, t_{\text{pulse}}, t_{\text{idle}}) = \frac{18M^2 t_{\text{pulse}}^2\left(\cos^2\phi + \cos^2\theta\sin^2\phi\right)}{\pi^2}, \quad (15)$$

which is zero only at $\pm\hat{y}$ (i.e., $\theta = \pi/2 = \pm\phi$, NZ1y) initializations. This result is consistent with the previous average Hamiltonian theory calculation. Going to finite frequency but in the limit of zero pulse width, we find that the magnetic noise filter function for NZ1y is given by

$$\mathcal{F}_{\mathcal{M}}^{\mathcal{I}}(\nu, M, t_{\text{pulse}} = 0, t_{\text{idle}}) = \frac{64(2+\cos(4\pi\nu t_{\text{idle}}))\cos^2(\pi\nu t_{\text{idle}})\sin^4(\pi\nu t_{\text{idle}})}{3\pi^2\nu^2} \times \frac{\sin^2(6M\pi\nu t_{\text{idle}})}{\sin^2(6\pi\nu t_{\text{idle}})} + \text{Larmor sideband terms.} \quad (16)$$

The Larmor sideband terms, as well as finite-pulse-width expressions, are elaborated in Appendix A. Example filter functions are shown in Fig. 2, where we plot the magnetic noise [Figs. 2(a) and 2(c)] and exchange noise [Figs. 2(b) and 2(d)] filter functions for differing numbers of repetitions and pulse timings.

The magnetic noise and exchange noise filter functions in Figs. 2(a) and 2(b), respectively, are plotted for differing numbers of six-pulse NZ repetitions M but fixed pulsing timing. Increasing the number of repetitions does not change the repetition frequency of this filter function, which is fixed at $1/6(t_{\text{pulse}} + t_{\text{idle}}) = 1/(6 \times 20 \text{ ns})$ and is shown as the dashed gray line. Instead, increasing M sharpens the filter function peaks. The filter functions in Figs. 2(c) and 2(d) are plotted with $M = 10$ and vary in

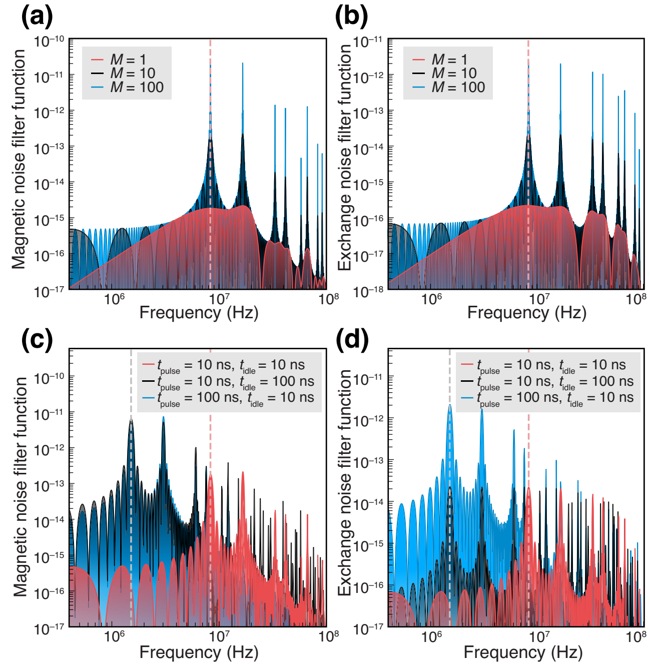

FIG. 2. Filter functions for infidelity of the NZ1y sequence construction. (a),(b) Magnetic noise and exchange noise filter functions for an $(\text{NZNZNZ})^M$ sequence with $t_{\text{pulse}} = 10$ ns and $t_{\text{idle}} = 10$ ns, and different sequence lengths $M = 1$, 10, and 100. The dashed gray line shows the repetition frequency of the sequence, which does not vary with M. (c),(d) Magnetic and exchange noise filter functions for $M = 10$ at several different durations t_{pulse} and t_{idle}. The dashed red line corresponds to the repetition frequency when $t_{\text{pulse}} = 10$ ns and $t_{\text{idle}} = 10$ ns. The repetition frequency is the same for the black and blue curves and is shown by the dashed gray line.

pulse timing. For the curves in red, the pulse repetition frequency is $1/(6 \times 20 \text{ ns})$ and is shown as the dashed red line. The black and blue curves share the same repetition frequency since $t_{\text{idle}} + t_{\text{pulse}}$ is the same for both filter functions, and its value is shown by the dashed gray line. From comparison of the magnetic noise and exchange noise filter functions in Figs. 2(c) and 2(d), respectively, it is clear that they have very different sensitivities to pulse timing. For the same value of $t_{\text{pulse}} + t_{\text{idle}}$, the magnetic noise filter function [the black and blue curves in Fig. 2(c)] is approximately the same amplitude. Magnetic error accumulates for the entirety of the pulse sequence and is insensitive to how the total sequence time is distributed between pulsing and idle. In contrast, Fig. 2(d) shows that while the central peak of the exchange noise filter function changes its frequency with $t_{\text{pulse}} + t_{\text{idle}}$, the amplitude of the filter function is dominated by the value of t_{pulse}. This is because exchange error accumulates only while a pulse is on.

When decoupling pulses are applied to a qubit, this analysis predicts an exponential decay in the probability of recovering the initial state upon repeated applications of the decoupling block. The rate of decay of the return probability with the number of decoupling pulses defines the NZ1y error, whose experimental measurement we discuss in the next section.

IV. EXPERIMENTAL RESULTS

We apply the two forms of first-order NZ sequences discussed above to our qubit, with results shown in Fig. 3. The experiments begin with initialization of spins to either the $|0\rangle$ state or the $|y\rangle$ state and culminate with a measurement of the $|0\rangle$ or $|y\rangle$ return probability upon ensemble average. In half of the experimental runs, a final X rotation is applied so that the ideal expected state is $|1\rangle$ or $|-y\rangle$, respectively. The sequence uses calibrated voltage pulses of duration $t_{\text{pulse}} = 10$ ns, with time between pulses $t_{\text{idle}} = 10$ ns. The initialization, measurement, and calibration methods are identical to those described in Ref. [18]. For the qubit in this work, a prepared state decays in $T_2^* = 2$ μs when device voltages are held in idle and no decoupling sequence is applied.

The first experiment aims to measure the NZ1 or NZ1z error by observing the decay in fidelity when the qubit is subjected to repeated applications of the decoupling block. For these experimental data, we track $r = 3M$, the number of repetitions of pairs of N and Z pulses; a full decoupling repetition occurs when r is a multiple of 3. Figure 3(a) shows the $|0\rangle$ and $|1\rangle$ return probabilities after $(NZ)^r$ pulses for $r = 0 \pmod 3$.

To extract both the error rate in the encoded space and the leakage to the $|Q\rangle$ state, we apply the same method as in "blind" randomized benchmarking [18], analyzing the sum and difference of the data traces for experiments with expected final states of $|0\rangle$ and $|1\rangle$ (see Appendix C). This is shown in Fig. 3(b), where we find that the NZ1 sequence results in an infidelity per exchange pulse $\epsilon_{\text{PP}} = 7.8 \times 10^{-4}$ and decay time $T_2 = 13$ μs. We attribute the extracted error per pulse to magnetic gradient noise that is accumulated during the finite-duration pulses, which may be reduced by use of the NZ1y sequence as discussed in Sec. III.

Hence, we apply the NZ1y sequence to the same qubit using the construction $\mathbb{SH}(NZ)^r\mathbb{HS}^\dagger$ and sweeping r with $r = 0 \pmod 3$ [Figs. 3(c) and 3(d)]. We find that the NZ1y sequence maintains qubit coherence for about 18 000 exchange pulses, equating to an infidelity per exchange pulse $\epsilon_{\text{PP}} = 2.8 \times 10^{-5}$. The decay time $T_2 = 360$ μs is about 28 times longer than that of the NZ1 sequence with the same pulse and idle durations. Additionally, as demonstrated by the sum curve, the NZ1y sequence does not exhibit any leakage into the $|Q\rangle$ state even for more than 200 000 exchange pulses, far after the encoded qubit has decohered. In comparison, blind randomized benchmarking performed on this qubit exhibited an error rate about 50 times higher (1.3×10^{-3} per pulse, with 2.7 pulses per Clifford operation), with magnetic noise contributing to half of the total error and a per-pulse leakage error of 6×10^{-4} [18].

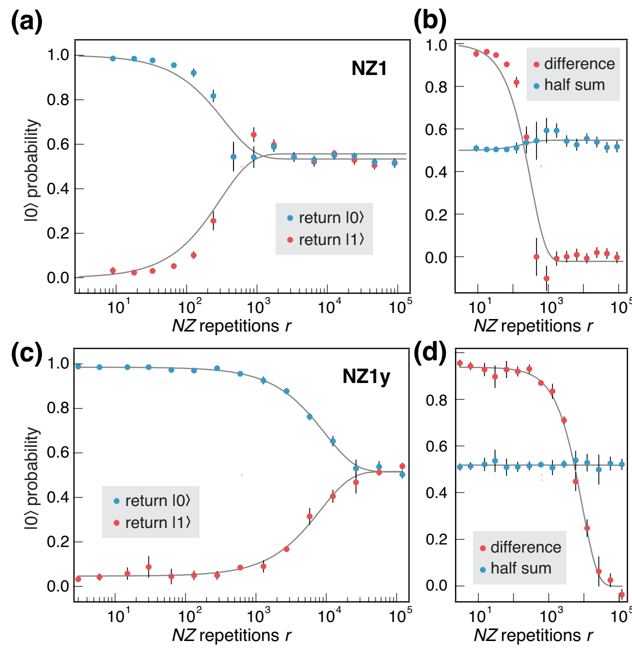

FIG. 3. Full-permutation DD of an encoded qubit. (a) NZ1 experiment results, plotting $|0\rangle$ return probability after the decoupling sequence of various lengths is applied. The ideal result is either 1 ($|0\rangle$ state, blue points) in half of the runs or 0 ($|1\rangle$ state, red points) in the other half due to an optionally applied X rotation. (b) Difference and sum curves. (c) NZ1y experiment results, in which the same decoupling sequence is applied to a state that is rotated by $\mathbb{SH}$ after preparation and $\mathbb{HS}^\dagger$ before measurement, again with both $|0\rangle$ and $|1\rangle$ expected final states. (d) The difference and the sum of the NZ1y data traces indicate error within and leakage out of the encoded subspace, respectively. A single-exponential fit to the difference curve yields a total error rate of 7.8×10^{-4} per pulse for the NZ1 sequence and 2.8×10^{-5} for the NZ1y sequence, with an indiscernible leakage rate for both sequences. Gray lines are fits to a single exponential constrained to probability < 1.

These results highlight how randomized benchmarking and the NZ1y experiments respond very differently to noise sources, allowing the latter to be a distinct, sensitive, and targeted probe of error contributions. In particular, we now study the effects of increasing the magnetic error contribution by increasing the idle duration in the NZ1y sequence. Although the passband locations of the magnetic noise and exchange noise filter functions depend on the total NZ1 block duration, the magnitude of the exchange noise filter function is insensitive to t_{idle}. This stems from the large on-off ratios achieved with the exchange interaction, with the result that the qubit suffers exchange noise from charge fluctuations only during t_{pulse}. Examining Figs. 2(c) and 2(d), we see that the magnetic noise and exchange noise filter functions have peaks in frequency space that are determined by the total $t_{\mathrm{pulse}} + t_{\mathrm{idle}}$, and that an increase in either t_{pulse} or t_{idle} is accompanied by an increase in magnitude of the magnetic noise filter function, whereas the exchange noise filter function amplitude is very sensitive to t_{pulse} only. Thus, sweeping t_{idle} can dramatically change the magnetic noise contribution, while having a smaller effect on the exchange noise contribution.

To this end, we perform a suite of NZ1y experiments, varying t_{idle} from 5 to 100 ns while keeping the pulse duration t_{pulse} constant at 10 ns. In doing so, we effectively sweep the primary NZ1y passband from 11 to 1.5 MHz, referring to the filter functions shown in Figs. 2(c) and 2(d). For each t_{idle}, we perform the experiment as in Fig. 3(d), extracting the total error and leakage error rates. The resulting rates are plotted in Fig. 4(a), and show that the error rate increases by about a factor of 5 over the range of the sweep. At short t_{idle}, the leakage error is less than 1/30 of the total error. At $t_{\mathrm{idle}} = 100$ ns, leakage error is significantly higher and magnetic noise contributes to 30% of the total error rate. In Fig. 4(b), we show the total decay time across the range, calculated as $T_2 = (t_{\mathrm{pulse}} + t_{\mathrm{idle}})/2\epsilon_{\mathrm{PP}}$, where ϵ_{PP} is the per-pulse error (see Appendix C). The arc in this plot elucidates a crossover between an exchange noise–dominated regime at short idle times and a magnetic noise–dominated regime at long idle times, where the filter function extends to include lower frequencies. We find a maximum T_2 of 720 μs at $t_{\mathrm{idle}} = 80$ ns.

To validate that the noise sources contributing to decay show the expected PSD frequency dependence of $1/f$, we also performed time-domain Monte Carlo simulations [18] of these NZ1y experiments across the range of differing t_{idle}. The simulation, with additional details described in Appendix E, includes a constant global magnetic field, B_0^z, and two noise sources: Magnetic noise [9,24,35] is composed of randomly oriented classical effective vector fields [nuclear polarization $\mathbf{b}_j$ in Sec. III, Eq. (2)] drawn from a $1/f$ power spectral density out to 10 kHz, beyond which it rolls off to $1/f^2$. This roll-off fits reasonably well with the data, although our data cannot determine its location with high accuracy. Charge noise is simulated by relative exchange fluctuations $\delta J_{jk}(t)/J_{jk}$ drawn from a $1/f$ distribution with high-frequency roll-off at >1 GHz. For both noise sources, low-frequency cutoffs to noise are selected to be lower than the inverse of the full experiment averaging time. The noise source amplitudes are calibrated via simulation of free-evolution [24] and triple-quantum-dot Rabi [25] experiments to reproduce the measured qubit parameters of $T_2^* = 2$ μs and 25 Rabi oscillations at $1/e$. Finally, we assume there is a global magnetic field B_0^z near the approximate value of Earth's field in Malibu, California. The experimental data show that both error and leakage increase near the Larmor resonance condition, and our simulation and filter function calculations capture this effect (the first-order average Hamiltonian analysis in Sec. III A does not).

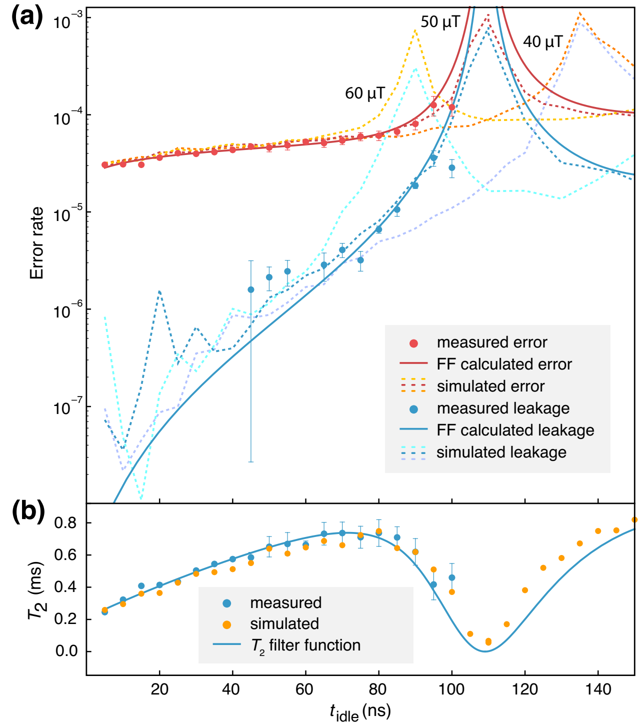

FIG. 4. NZ1y sequence with variable idle time. (a) Measured, simulated, and calculated error and leakage per pulse as a function of swept t_{idle}. Simulation results (dotted lines) are shown at three different values of B_0^z to show the effect of Larmor resonance. Analytic calculations [solid lines, Eqs. (D14) and (D17)] integrating the filter functions (FFs) with the assumed noise spectra are performed at $B_0^z = 50$ μT, matching the experimental data. (b) Extracted T_2 decay time for each measured sequence reveals a maximum T_2 of 720 μs at $t_{\mathrm{idle}} = 80$ ns.

The simulation results for several field values are shown as dashed lines in Fig. 4 and have good correspondence with the experimental data for the case of $B_0^z = 50$ μT. An increase in measured error seen near $t_{\mathrm{idle}} = 95$ ns is ascribed to pulsing near resonance with the electron Larmor frequency, $g\mu_B B_0^z/h$. In addition to the simulation, an analytic calculation (solid line) integrating the filter function with the assumed noise spectra was also performed (see Appendix D), with the best match to the experimental data also found at $B_0^z = 50$ μT. The extended coherence of this sequence allows validation of our noisy exchange simulator (and its assumed noise spectra) at greater values of the operating fidelity than were accessible by randomized benchmarking [18].

V. CONCLUSION

We have experimentally demonstrated the full-permutation dynamical decoupling sequence in an exchange-only triple-quantum-dot qubit. The NZ1y sequence features an exceptionally low error rate of 2.8×10^{-5} per pulse when applied to our qubit, which is attributed to effective echoing of magnetic noise and suppression of low-frequency fluctuations in both exchange and local magnetic fields. Additionally, because of strong insensitivity to pulse miscalibration, the sequence allows the $1/f$ noise tail and any high-frequency noise processes to be examined independently of calibration accuracy. The resulting maximum coherence time $T_2 = 720$ μs is comparable to that previously measured at high magnetic field via double-quantum-dot permutation [9], as well as to the 870 μs shown with multipulse double-quantum-dot exchange decoupling in AlGaAs/GaAs [36], which itself extended a prior AlGaAs/GaAs result of 200 μs [37]. The result we have presented here differs operationally from the results in both these prior studies not only for its full permutation in a triple quantum dot, but also in being obtained in the low external field regime of $B_0 = 50$ μT provided only by Earth. Although our key goal here is validation of our noise model, coherence time can be an important metric by itself, for example, for quantum memory, and further increases of the coherence time relative to the present result could be achieved by operation at higher external fields, with devices exhibiting lower exchange noise, or with increased isotopic enhancement.

Our simulations accurately account for the measured error and leakage rates in this experiment. We have studied how extending t_{idle} increases both error within and leakage out of the DFS by increasing susceptibility to magnetic fluctuations, as is clear from the calculable filter function, and we find agreement with time-domain simulation. The NZ1y sequence has proven exceptionally helpful in validating our error model for this qubit, and we expect the sequence's continued utility as exchange-only qubits improve thanks to advancements such as the SLEDGE architecture [29,38]. We have also found that permutational dynamical decoupling can be combined with exchange-only quantum logic, potentially enabling new avenues for exchange-only logic robust with regard to random magnetic field gradients [39,40]. When qubit swapping has strong enough control fidelity, permutation decoupling may be similarly valuable for preserving coherence and validating error models in other platforms, such as higher-spin-orbit-coupling materials, including hole qubits, and superconducting qubits. Quiroz et al. [41] also demonstrated three-physical-qubit permutational dynamical decoupling with SWAP gates constructed from controlled-NOT gates in the IBM superconducting qubit Montreal device, finding that DD on DFS-encoded qubits outperforms "bare" physical qubits, DD on physical qubits, and DFS encoding alone. Finally, bounded control schemes can also be devised for exchange-only decoupling [42], with suitably derived optimal pulse shapes [43], although the short-π-pulse or nearest-neighbor transposition implementation presented here has the most straightforward interpretation as permuting over S_3.

ACKNOWLEDGMENTS

We thank John Carpenter for assistance with all figures. We acknowledge Cody Jones and Tyler Keating for significant technical contributions.

APPENDIX A: SEQUENCE FILTER FUNCTIONS

In this appendix, we compute filter functions for the NZ sequences discussed in the main text. Filter functions are computed in first-order Magnus-expansion perturbation theory, which is sufficient to compute state preservation and orthogonal state transition probabilities to second order in the noise.

We mathematically separate noise by first defining the noiseless Hamiltonian $H_0(t)$ to include $H_{\text{control}}(t)$, as in Eq. (1), under the assumption of perfectly calibrated, nonoverlapping square pulses for $J_{12}(t)$ and $J_{23}(t)$, as well as a uniform, constant applied magnetic field, $\mathbf{B}_0$, explicitly

$$H_0(t) = H_{\text{control}}(t) - g\mu_B \mathbf{B}_0 \cdot \mathbf{S}, \tag{A1}$$

with total spin $\mathbf{S} = \sum_j \mathbf{S}_j$ as before. We further introduce the shorthand Larmor frequency $\nu_0 = |g\mu_B \mathbf{B}_0|/h$. As all terms in Eq. (A1) commute, it is straightforward to integrate

$$U_0(t) = \exp\left(-\frac{i}{\hbar}\int_0^t d\tau H_0(\tau)\right), \tag{A2}$$

which we use to classify terms in the time integral of the interaction picture noise Hamiltonian $H_{\text{noise}}(t)$ from Eq. (4) as

$$\Xi(t) = \frac{1}{\hbar}\int_0^t d\tau\ U_0^\dagger(\tau) H_{\text{noise}}(\tau) U_0(\tau) = \sum_j \mathbf{S}_j \cdot \mathbf{u}_j(t) - \sum_{\boldsymbol{\alpha}} \mathbf{S}_{\alpha_1} \times \mathbf{S}_{\alpha_2} \cdot \mathbf{v}_{\alpha_3}(t) + \mathbf{S}_{\alpha_1} \cdot \mathbf{S}_{\alpha_2} w_{\alpha_3}(t). \tag{A3}$$

Here we use the vector of subscripts $\boldsymbol{\alpha}$ for enumeration over the ordered sets of quantum dot indices $\{[1,2,3],[2,3,1],[3,1,2]\}$. We have thus sorted terms into error phase angle integrals given by

$$\mathbf{u}_j(t) \equiv \int_0^t d\tau\ \sum_k f_{jk}(\tau)\mathbf{R}(\tau)\cdot \mathbf{b}_k(\tau), \tag{A4}$$

$$\mathbf{v}_j(t) \equiv \int_0^t d\tau\ \sum_{k\ell m} g_{jk}(\tau)\epsilon_{\ell k m}\mathbf{R}(\tau)\cdot \mathbf{b}_m(\tau), \tag{A5}$$

$$w_j(t) \equiv \int_0^t d\tau\ \sum_{\boldsymbol{\alpha}} \delta J_{\alpha_1\alpha_2}(\tau) h_{j\alpha_3}(\tau). \tag{A6}$$

The error phase angle expressions have straightforward physical explanations: the magnetic error phases $\mathbf{u}_j(t)$, for example, include external magnetic field–generated Larmor precession through the spatial rotation matrix

$$\mathbf{R}(t) \equiv \begin{pmatrix} \cos(2\pi\nu_0 t) & \sin(2\pi\nu_0 t) & 0 \\ -\sin(2\pi\nu_0 t) & \cos(2\pi\nu_0 t) & 0 \\ 0 & 0 & 1 \end{pmatrix} \tag{A7}$$

and π pulse–induced permutations through the "switching" matrices $f_{jk}(t)$, which in the zero-width-exchange-pulse limit are natural permutation representation matrices of the symmetric group S_3 corresponding to a particular sequence of N and Z pulses. For finite-width exchange pulses, the $f_{jk}(t)$ also include transitional matrices giving the time dependence of the mapping of Pauli spin matrices from one quantum dot to another as exchange is applied. The finite exchange pulse width additionally gives rise to a weight-2 Pauli term reflected as $\mathbf{v}_j(t)$, with $g_{jk}(s)$ another set of switching matrices that can be determined from $f_{jk}(s)$ through a masking procedure, and $\epsilon_{jk\ell}$ is the Levi-Civita tensor. Exchange error phases $w_j(t)$ similarly have switching matrices $h_{jk}(t)$ that are determined from $f_{jk}(t)$.

Using our previously introduced basis notation $|S_{12}, S; m\rangle$, we enumerate the eight-state basis as follows. The encoded states (duplicated twice due to gauge freedom) are the first four states:

$$\begin{aligned}
|1\rangle &\equiv \cos\frac{\theta}{2}\,|0, 1/2; +1/2\rangle + \sin\frac{\theta}{2}e^{i\phi}\,|1, 1/2; +1/2\rangle\,, \\
|2\rangle &\equiv \cos\frac{\theta}{2}\,|0, 1/2; -1/2\rangle + \sin\frac{\theta}{2}e^{i\phi}\,|1, 1/2; -1/2\rangle\,, \\
|3\rangle &\equiv \sin\frac{\theta}{2}\,|0, 1/2; +1/2\rangle - \cos\frac{\theta}{2}e^{i\phi}\,|1, 1/2; +1/2\rangle\,, \\
|4\rangle &\equiv \sin\frac{\theta}{2}\,|0, 1/2; -1/2\rangle - \cos\frac{\theta}{2}e^{i\phi}\,|1, 1/2; -1/2\rangle\,,
\end{aligned}$$

where θ and ϕ specify the Bloch-sphere polar angles of the encoded state, which we alter according to the experiment we choose to analyze. The remaining four states are the leakage quadruplet,

$$\begin{aligned}
|5\rangle &\equiv |1, 3/2; +3/2\rangle\,, \\
|6\rangle &\equiv |1, 3/2; +1/2\rangle\,, \\
|7\rangle &\equiv |1, 3/2; -1/2\rangle\,, \\
|8\rangle &\equiv |1, 3/2; -3/2\rangle\,,
\end{aligned}$$

collectively abbreviated as $|Q\rangle$. Assuming that the initial encoded state is totally mixed in gauge, all probabilities of interest can be written as

$$P(t) = \frac{1}{2}\left\langle \sum_f \sum_{i=1}^{2} \left|\langle f|\, U_0(t)\tilde{U}_{\mathrm{noise}}(t)\,|i\rangle\right|^2 \right\rangle, \tag{A8}$$

where $\tilde{U}_{\mathrm{noise}}(t)$ is the interaction propagator for $H_{\mathrm{noise}}(t)$ under $H_0(t)$, and the outer brackets $\langle\cdot\rangle$ refer to ensemble averaging over noise terms. We define the "state preservation probability" $P_I(t)$ for which the final states to be summed over are $|f\rangle \in \{|1\rangle, |2\rangle\}$; we also define the "encoded error probability" for which $|f\rangle \in \{|3\rangle, |4\rangle\}$. The "leakage error probability" would have $|f\rangle \in \{|5\rangle, |6\rangle, |7\rangle, |8\rangle\}$. Assuming that the sequence of N and Z pulses results in the identity, $U_0(t)$ acts trivially to the left on $\langle f|$ states, so all probabilities depend only on the interaction propagator. Therefore, to lowest order in the Magnus expansion, all probabilities take the form

$$P(t) \approx \left\langle \sum_{i,f} \left|\langle f|\left[1 - i\Xi(t) - \frac{1}{2}\Xi^2(t)\right]|i\rangle\right|^2 \right\rangle, \tag{A9}$$

which is correct to second order in the noise.

Substituting Eq. (A3) into Eq. (A9), with the assumptions that the noise has zero mean and that magnetic and exchange errors are uncorrelated, we arrive at quadratic terms of the form

$$\begin{aligned}
\mathcal{Q} = \sum_{jk} & Q^{(11)}_{\mathcal{M},jk}(\theta,\phi)\left\langle \mathbf{u}_j \cdot \mathbf{u}_k\right\rangle + Q^{(12)}_{\mathcal{M},jk}(\theta,\phi)\left\langle \mathbf{u}_j \cdot \mathbf{v}_k\right\rangle \\
&\times Q^{(21)}_{\mathcal{M},jk}(\theta,\phi)\left\langle \mathbf{v}_j \cdot \mathbf{u}_k\right\rangle + Q^{(22)}_{\mathcal{M},jk}(\theta,\phi)\left\langle \mathbf{v}_j \cdot \mathbf{v}_k\right\rangle \\
&+ Q_{\mathcal{E},jk}(\theta,\phi)\left\langle w_j w_k\right\rangle,
\end{aligned} \tag{A10}$$

where the error phase angles are given in Eqs. (A4)–(A6), and the angle brackets are noise averages. The Q matrices are dependent on the encoded initial state parameters θ and ϕ, and they differ for each of the three probabilities of interest. For state preservation probability, $P_S = 1 - \mathcal{Q}$; for encoded and leakage error probabilities, $P_{E,L} = \mathcal{Q}$, with suitable substitutions for the different Q matrices. The quadratic magnetic-error-phase-angle noise average, under the assumption that random noise fields at different quantum dots and along different axes are uncorrelated and identically distributed with correlation function $\langle b(\tau_1)b(\tau_2)\rangle$, is given by

$$\begin{aligned}
\langle \mathbf{u}_j \cdot \mathbf{u}_k\rangle &= \int_0^t d\tau_1 \int_0^t d\tau_2 \sum_{\ell m} f_{j\ell}(\tau_1) f_{km}(\tau_2)\, \langle \mathbf{b}_\ell(\tau_1) \\
&\quad \cdot \mathbf{R}^T(\tau_1) \cdot \mathbf{R}(\tau_2) \cdot \mathbf{b}_m(\tau_2)\rangle \\
&= \int_0^t d\tau_1 \int_0^t d\tau_2\, \mathrm{Tr}[\mathbf{R}^T(\tau_1)\mathbf{R}(\tau_2)]\langle b(\tau_1)b(\tau_2)\rangle \\
&\quad \times \sum_\ell f_{j\ell}(\tau_1) f_{k\ell}(\tau_2)
\end{aligned}$$

$$= \int_0^t d\tau_1 \int_0^t d\tau_2 \, [1 + 2\cos(2\pi\nu_0(\tau_1 - \tau_2))] \times \int_0^\infty d\nu S_B(\nu) \cos[2\pi\nu(\tau_1 - \tau_2)] \times \sum_\ell f_{j\ell}(\tau_1) f_{k\ell}(\tau_2). \tag{A11}$$

The final equality uses the Wiener-Khinchin theorem, with $S_B(\nu)$ the one-sided magnetic noise power spectral density for any component $\mathbf{b}_j(t)$ in any quantum dot. We now define the Fourier-like transform of the switching matrices:

$$\tilde{f}_{jk}(\nu, t) \equiv \int_0^t d\tau \, e^{-2\pi i \nu \tau} f_{jk}(\tau). \tag{A12}$$

Performing the sum over the Larmor rotation matrices and using the symmetry property of the $Q^{(11)}_{\mathcal{M},jk}$ matrix, we may write

$$Q^{(11)}_{\mathcal{M},jk} \langle \mathbf{u}_j \cdot \mathbf{u}_k \rangle = Q^{(11)}_{\mathcal{M},jk} \int_0^\infty d\nu \, S_B(\nu) \times \sum_\ell \Big[\tilde{f}_{j\ell}(\nu, t) \tilde{f}^*_{k\ell}(\nu, t) + \tilde{f}_{j\ell}(\nu + \nu_0, t) \times \tilde{f}^*_{k\ell}(\nu + \nu_0, t) + \tilde{f}_{j\ell}(\nu - \nu_0, t) \tilde{f}^*_{k\ell}(\nu - \nu_0, t) \Big]. \tag{A13}$$

All terms to the right of $S_B(\nu)$ are the (weight-1 Pauli) magnetic error phase contribution to the magnetic noise filter function. As with other filter function analyses [9], the filter function is the squared magnitude of the Fourier transform of a switching function, with geometric factors arising from the initial state. The finite external magnetic field introduces sideband contributions to the filter function; in the limit of large field, these contributions go to zero. The remaining quadratic-error phase-average terms in Eq. (A10) all have the same structure as Eq. (A13) with different quadratic combinations of $\tilde{f}$, $\tilde{g}$, and $\tilde{h}$, and include the effects of weight-2 Pauli finite-pulse-width magnetic errors as well as exchange errors.

Combining the algebra and definitions above, we now summarize the total approximate state preservation probability, given by

$$P_S \approx 1 - \int_0^\infty d\nu \, S_B(\nu) \mathcal{F}^{\mathcal{I}}_{\mathcal{M}}(\theta, \phi, \nu, M, t_{\rm pulse}, t_{\rm idle}) - \int_0^\infty d\nu \, S_E(\nu) \mathcal{F}^{\mathcal{I}}_{E}(\theta, \phi, \nu, M, t_{\rm pulse}, t_{\rm idle}), \tag{A14}$$

where $\mathcal{F}^{\mathcal{I}}_{\mathcal{M}}$ is the magnetic noise filter function for state preservation infidelity, which is dependent on the initial state parameters θ and ϕ, as well as the frequency ν, the number of repetitions M of the six-pulse NZ1 sequence, and the pulse width $t_{\rm pulse}$ and idle time between pulses $t_{\rm idle}$; $S_E(\nu)$ is the exchange noise power spectral density; and $\mathcal{F}^{\mathcal{I}}_{E}$ is the exchange noise filter function for state preservation infidelity. Writing the pulse width and idle time in terms of the fractional pulse width $f = t_{\rm pulse}/\tau$ and pulse repetition time $\tau = t_{\rm pulse} + t_{\rm idle}$, we have the NZ1y magnetic noise filter function for state preservation infidelity:

$$\begin{aligned}
\mathcal{F}^{\mathcal{I}}_{\mathcal{M}}(\pi/2, \pi/2, \nu, M, f\tau, (1-f)\tau) &= \frac{1}{6\pi^2\nu^2\left(1 - 4f^2\nu^2\tau^2\right)^2} \frac{\sin^2(6M\pi\nu\tau)}{\sin^2(6\pi\nu\tau)} \\
&\times \Big\{7 + 32 f^4\nu^4\tau^4 + 16\left(4f^2\nu^2\tau^2 - 1\right)\sin^3(\pi\nu\tau)\cos^2(\pi\nu\tau)(2\cos(4\pi\nu\tau) + 1)\sin(2\pi f\nu\tau) \\
&\times \left(-\sqrt{3} f\nu\tau \sin(\pi\nu\tau) + \cos(\pi\nu\tau) + 2\cos(3\pi\nu\tau)\right) \\
&+ f\nu\tau\Big[f\nu\tau\Big(2f\nu\tau\left(-16 f\nu\tau\cos(12\pi\nu\tau) - 4\sqrt{3}\sin^3(2\pi\nu\tau)(2\cos(4\pi\nu\tau) + 1)\right) \\
&+ \cos(2\pi\nu\tau) - 8\cos(4\pi\nu\tau) + 6\cos(6\pi\nu\tau) - 4\cos(8\pi\nu\tau) - 7\cos(10\pi\nu\tau) + 12\cos(12\pi\nu\tau)\Big) \\
&+ 2\sqrt{3}\sin^3(2\pi\nu\tau)(-16\cos(2\pi\nu\tau) + 6\cos(4\pi\nu\tau) + 7)\Big] \\
&+ 2\sin^2(2\pi\nu\tau)\cos(2\pi f\nu\tau)\Big[f\nu\tau\Big(2f\nu\tau\Big(-2\sqrt{3} f\nu\tau\sin(6\pi\nu\tau) + 8\cos(2\pi\nu\tau) \\
&+ 12\cos(4\pi\nu\tau) + 7\cos(6\pi\nu\tau) + 4\cos(8\pi\nu\tau) + 14\Big) + \sqrt{3}(4\sin(2\pi\nu\tau) \\
&- 8\sin(4\pi\nu\tau) + 3\sin(6\pi\nu\tau))\Big) - 10\cos(2\pi\nu\tau) - 2\cos(6\pi\nu\tau) - 2\cos(8\pi\nu\tau) + 5\Big] \\
&- 4\cos(2\pi\nu\tau) - 4\cos(4\pi\nu\tau) + 3\cos(6\pi\nu\tau) - 2\cos(8\pi\nu\tau) + \cos(10\pi\nu\tau) - \cos(12\pi\nu\tau)\Big\} + \text{sideband terms},
\end{aligned} \tag{A15}$$

where the sideband terms are determined from the displayed expression by the substitutions $\nu \to \nu \pm \nu_0$. The NZ1y exchange noise filter function for state preservation infidelity is given by

$$\mathcal{F}_E^{\mathcal{I}}(\pi/2, \pi/2, \nu, M, t_{\text{pulse}}, t_{\text{idle}}) = \frac{2(2+\cos 4\pi\nu\tau)\sin^2(\pi\nu t_{\text{pulse}})\sin^2(2\pi\nu\tau)}{\pi^2\nu^2}\frac{\sin^2(6M\pi\nu\tau)}{\sin^2(6\pi\nu\tau)}, \tag{A16}$$

which has no sideband contributions and $\tau = t_{\text{idle}} + t_{\text{pulse}}$. The main (not sideband) NZ1y magnetic noise filter function at zero frequency ($\nu = 0$) is zero, consistent with the average Hamiltonian theory result in the main text.

In general, the arbitrary initial state magnetic noise filter function at $\nu = 0$ is given by (ignoring sideband terms)

$$\mathcal{F}_{\mathcal{M}}^{\mathcal{I}}(\theta, \phi, 0, M, t_{\text{pulse}}, t_{\text{idle}}) = \frac{18M^2 t_{\text{pulse}}^2\left(\cos^2\phi + \cos^2\theta\sin^2\phi\right)}{\pi^2}, \tag{A17}$$

which is zero only for y-axis initialization (i.e., $\theta = \pi/2 = \pm\phi$). Initializations in other directions quadratically (coherently) accumulate finite-pulse-width, zero-frequency magnetic noise errors under NZ pulsing.

In the limit of zero pulse width, the magnetic noise filter function for NZ1y is as follows:

$$\mathcal{F}_{\mathcal{M}}^{\mathcal{I}}(\pi/2, \pi/2, \nu, M, 0, t_{\text{idle}}) = \frac{64(2+\cos 4\pi\nu t_{\text{idle}})\cos^2(\pi\nu t_{\text{idle}})\sin^4(\pi\nu t_{\text{idle}})}{3\pi^2\nu^2}\frac{\sin^2(6M\pi\nu t_{\text{idle}})}{\sin^2(6\pi\nu t_{\text{idle}})} + \text{sideband terms.} \tag{A18}$$

The corresponding zero-pulse-width exchange noise filter function is, of course, zero.

The approximate encoded error probability for NZ1y, i.e., the probability of flipping between encoded qubit states (without leakage), is given by

$$P_E = \int_0^\infty d\nu\, S_B(\nu)\mathcal{F}_{\mathcal{M}}^{\mathcal{E}}(\theta, \phi, \nu, M, t_{\text{pulse}}, t_{\text{idle}}) + \int_0^\infty d\nu\, S_E(\nu)\mathcal{F}_E^{\mathcal{I}}(\theta, \phi, \nu, M, t_{\text{pulse}}, t_{\text{idle}}), \tag{A19}$$

with the encoded error magnetic noise filter function given by

$$\begin{aligned}
\mathcal{F}_{\mathcal{M}}^{\mathcal{E}}(\pi/2, \pi/2, \nu, M, f\tau, (1-f)\tau) &= \frac{1}{12\pi^2\nu^2\left(1-4f^2\nu^2\tau^2\right)^2}\frac{\sin^2(6M\pi\nu\tau)}{\sin^2(6\pi\nu\tau)}\\
&\times \big[7 + 32f^4\nu^4\tau^4 - 32f^4\nu^4\tau^4\cos(12\pi\nu\tau) - 12f^2\nu^2\tau^2 + 6f^2\nu^2\tau^2(\cos(2\pi\nu\tau) - \cos(10\pi\nu\tau) + 2\cos(12\pi\nu\tau))\\
&+ 2\sin^2(2\pi\nu\tau)\big\{\left(4f^2\nu^2\tau^2 - 1\right)(2\sin(4\pi\nu\tau) - \sin(6\pi\nu\tau) + 2\sin(8\pi\nu\tau))\sin(2\pi f\nu\tau)\\
&+ \big(4f^2\nu^2\tau^2(6\cos(2\pi\nu\tau) + 4\cos(4\pi\nu\tau) + 3\cos(6\pi\nu\tau) + 2\cos(8\pi\nu\tau) + 3)\\
&- 10\cos(2\pi\nu\tau) - 2\cos(6\pi\nu\tau) - 2\cos(8\pi\nu\tau) + 5\big)\cos(2\pi f\nu\tau)\big\}\\
&- 4\cos(2\pi\nu\tau) - 4\cos(4\pi\nu\tau) + 3\cos(6\pi\nu\tau) - 2\cos(8\pi\nu\tau) + \cos(10\pi\nu\tau) - \cos(12\pi\nu\tau)\big] + \text{sideband terms.}
\end{aligned} \tag{A20}$$

Notice that the encoded error exchange noise filter function is the same as the exchange noise filter function for state preservation infidelity since exchange errors do not cause leakage. The remaining leakage error magnetic noise filter function is the difference of the state preservation infidelity and encoded error filter functions.

APPENDIX B: NONRECTANGULAR PULSES

We now discuss the effect of nonrectangular exchange pulses on the NZ1 filter function response. For simplicity, we consider here the case of exchange noise, $\mathcal{F}_E^{\mathcal{I}}$. Nonrectangular pulse shapes correspond to varying noise sensitivity over the duration of the exchange pulse, which can qualitatively modify the filter function envelope. The exchange pulse shape enters the filter function expression in Eq. (A16) via the switching terms $h_{jk}(t)$ defined in Eq. (A6), which encode the time-dependent mapping of Pauli spin matrices over the NZ1 sequence. Assuming all pulses have the same shape, the integral over these switching terms is separable into two components corresponding to the pulse shape and the pulses' relative time shifts over the NZ1 sequence. Specific to NZ1y, we find that

$$\mathcal{F}_E^{\mathcal{I}} = 2|h_{\text{pulse}}(\nu, t_{\text{pulse}})|^2 (2 + \cos 4\pi\nu\tau) \sin^2(2\pi\nu\tau) \times \frac{\sin^2(6M\pi\nu\tau)}{\sin^2(6\pi\nu\tau)}. \quad \text{(B1)}$$

For a rectangular pulse with duration t_{pulse},

$$h_{\text{rect}}\left(\nu, t_{\text{pulse}}\right) = \frac{i}{2\pi\nu}\left(e^{-i2\pi\nu t_{\text{pulse}}} - 1\right) \quad \text{(B2)}$$

and we recover the results of Eq. (A16). For a trapezoidal voltage pulse with ramp time t_R, full-width-half-maximum t_{pulse}, on-off ratio α between minimum and maximum sensitivity values, and an exponential scaling between exchange energy and voltage,

$$\begin{aligned} h_{\text{trapez}}\left(\nu, t_{\text{pulse}}\right) = &\frac{1}{\alpha}\frac{i}{2\pi(\nu + i\nu_R)}\left(e^{-i2\pi(\nu+i\nu_R)t_R} - 1\right) \\ &+ \frac{i}{2\pi\nu}\left(e^{-i2\pi\nu t_{\text{pulse}}} - e^{-i2\pi\nu t_R}\right) \\ &+ \frac{ie^{-i2\pi\nu t_{\text{pulse}}}}{2\pi(\nu - i\nu_R)}\left(e^{-i2\pi(\nu-i\nu_R)t_R} - 1\right), \end{aligned} \quad \text{(B3)}$$

where $2\pi\nu_R = (1 - 1/\alpha)/t_R$. Compared with rectangular pulses, this filter envelope has a higher frequency cutoff but with a faster decay rate.

APPENDIX C: FITTING ERROR AND LEAKAGE RATES

To fit our data and extract the error rates, we follow the same procedure as outlined in Ref. [18]. We construct two different NZ1 sequences with expected return to the $|0\rangle$ state and the $|1\rangle$ state, in the case of NZ1 and NZ1z, and with expected return to $|y\rangle$ and $|-y\rangle$ in the case of NZ1y. The probability of returning to $|0\rangle$ or $|y\rangle$ when so expected is given by $y_0(M)$. To detect leakage, we also examine the sequences with expected return to $|1\rangle$ or $|-y\rangle$, constructed by our simply appending a composite X gate, implemented as in Ref. [18]. The $|0\rangle$ return probability of such an inverted sequence is assigned to $y_1(M)$. We use the ansatz

$$\begin{aligned} y_0(M) &= A + B(1-p)^M + C(1-q)^M, \\ y_1(M) &= A - B(1-p)^M + C(1-q)^M, \end{aligned} \quad \text{(C1)}$$

where M is the number of repetitions of the six-pulse NZ1 sequence, and we fit separate exponentials to $y_0 - y_1$ and $(y_0 + y_1)/2$ to estimate the parameters A, B, C, p, and q. At $M \to 0$, $y_0 - y_1$ approaches $2B$. As this difference represents the probability of measuring $|0\rangle$ or $|1\rangle$ immediately after preparation (and noting that leakage states $|Q\rangle$ also measure as $S_{12} = 1$), this quantity would be unity were it not for state preparation and measurement error. Therefore, we take $2B$ as the probability that a singlet state or a triplet state in the two measured spins measures correctly, and we divide by this probability to get the total error. Our total error per definition equation (11) would be

$$\begin{aligned} \epsilon &= \lim_{M\to\infty} \frac{1}{M}\left[1 - \frac{A}{2B} - \frac{1}{2}(1-p)^M - \frac{C}{2B}(1-q)^M\right] \\ &\approx \frac{p}{2} + \frac{Cq}{2B}. \end{aligned} \quad \text{(C2)}$$

The approximation is under both the assumption of $p, q \ll 1$ and the accuracy of the ansatz, the latter of which we discuss shortly. For the leakage rate, an unleaked state would always be inverted and hence $y_0 + y_1$ would sum to unity. The probability that it does not after M six-pulse repetitions is approximately $1 - (2C(1-q)^M)/2B$, again with normalization by the probability that we measured correctly, leading to the limiting rate at $q \ll 1$ of

$$\Gamma = \frac{Cq}{B}. \quad \text{(C3)}$$

These definitions are consistent with those in Ref. [18], with the notable difference in interpretation that in Ref. [18] an average process infidelity under a depolarization error model enforced by Clifford twirling is sought, whereas the expressions above correspond to a state return error per Eq. (11) without our imposing or assuming a depolarization error model.

We consider for convenience the error and leakage per pulse, ϵ_{PP} and Γ_{PP}; the error and leakage for the NZ1y experiment are $\epsilon_{\text{NZ1y}} = \epsilon$ and $\Gamma_{\text{NZ1y}} = \Gamma$ when the initial state is $|y\rangle$. They are simply related by the number of pulses per constituent sequence, i.e., $\epsilon_{\text{NZ1y}} = 6\epsilon_{\text{PP}}$ and $\Gamma_{\text{NZ1y}} = 6\Gamma_{\text{PP}}$. A final definition used is T_2 under repeated NZ1 sequences, which is, by standard definition of T_2, the total time it takes for the return probability of the initial state to fall to $1/e$. From the definition of y_0 and for small enough error, this is easily seen to be

$$\begin{aligned} T_2 &= (t_{\text{pulse}} + t_{\text{idle}})/2\epsilon_{\text{PP}} \\ &= 3(t_{\text{pulse}} + t_{\text{idle}})/\epsilon_{\text{NZ1y}}. \end{aligned} \quad \text{(C4)}$$

Equations (C2) and (C3) should be considered a definition of leakage and total error as measured by our "blind" protocol. Theoretically, we use a noise model with each interval's noise static and independent, i.e., evolution within an interval is coherent but is Markovian from interval to interval. (A white magnetic noise model cannot be used for the analysis as zero magnetic noise correlation time eliminates Larmor precession effects—the noise is infinitely faster than the Larmor frequency.) Each exchange gate's noise is assumed to be independent and identically distributed as is each component of each quantum dot's magnetic noise. Computing noise-averaged process matrices for this model and taking components corresponding to NZ1y probabilities, we obtain

$$y_0(M) = \frac{1}{4} + \frac{1}{2}(1-p)^M + \frac{1}{6}(1-q_1)^M + \frac{1}{12}(1-q_2)^M,$$
$$y_1(M) = \frac{1}{4} - \frac{1}{2}(1-p)^M + \frac{1}{6}(1-q_1)^M + \frac{1}{12}(1-q_2)^M,$$
$$y_2(M) = \frac{1}{4} - \frac{1}{3}(1-q_1)^M + \frac{1}{12}(1-q_2)^M,$$
$$y_3(M) = \frac{1}{4} - \frac{1}{4}(1-q_2)^M,$$

where y_2 would, analogously to y_1, be the singlet probability measured if we could append a pulse sequence that converted the $|Q\rangle$ leakage states with $m = \pm 1/2$ to $|0\rangle$ before measurement, and y_3 would be the singlet probability measured if could append a sequence that converted the $|Q\rangle$ states with $m = \pm 3/2$ to $|0\rangle$. As these sequences do not exist, y_2 and y_3 are theoretical, to give a more comprehensive picture of probabilities. Matching the Markovian noise model theory at low error rates with the filter function theory gives

$$p = 6 \times \left(2\epsilon_{\mathrm{PP},E} + 3(\Gamma_{\mathrm{PP},0} + \Gamma_{\mathrm{PP},+} + \Gamma_{\mathrm{PP},-})\right)$$
$$q_1 = 6 \times 3\left(\Gamma_{\mathrm{PP},0} + \frac{1}{2}(\Gamma_{\mathrm{PP},+} + \Gamma_{\mathrm{PP},-})\right)$$
$$q_2 = 6 \times 3\left(\Gamma_{\mathrm{PP},+} + \Gamma_{\mathrm{PP},-}\right),$$

where $\epsilon_{\mathrm{PP},E}$ and $\Gamma_{\mathrm{PP},s}$ are defined with use of the filter functions in Appendix A:

$$\epsilon_{\mathrm{PP},E} = \lim_{M\to\infty} \frac{1}{6M} \int_0^\infty d\nu S_E(\nu)\mathcal{F}_E^{\mathcal{I}}(\nu), \tag{C5}$$
$$\Gamma_{\mathrm{PP},s} = \lim_{M\to\infty} \frac{1}{6M} \int_0^\infty d\nu S_B(\nu)\mathcal{F}_{\mathcal{M},0}^{\mathcal{L}}(\nu + s\nu_0), \tag{C6}$$

where $\mathcal{F}_{\mathcal{M},0}^{\mathcal{L}}$ is the magnetic leakage filter function without sideband terms. Approximate analytic expressions for $\epsilon_{\mathrm{PP},E}$, Eq. (D9), and $\Gamma_{\mathrm{PP},s}$, Eqs. (D15) and (D16), are computed in Appendix D. Recall that the Larmor sideband terms at $s = \pm 1$ ultimately arise from gradients in the magnetic field direction, i.e., from the $S^x b^x(t) + S^y b^y(t)$ terms of the magnetic noise Hamiltonian, which precess in the interaction picture at the Larmor frequency ν_0. These lead to additional modified leakage rates $\Gamma_{\mathrm{PP},\pm}$. At very high magnetic field, in which ν_0 is large, the filter function's $1/\nu^2$ dependence makes $\Gamma_{\mathrm{PP},\pm}$ small. At low field, depending on the pulse period τ, $\Gamma_{\mathrm{PP},\pm}$ are generally comparable to or, at Larmor resonances, much larger than $\Gamma_{\mathrm{PP},0}$.

At high magnetic field, $q_2 = 0 = \Gamma_{\mathrm{PP},\pm}$, our theoretical expressions for y_0 and y_1 match our ansatz equation (C1), with $A = 1/3, B = 1/2, C = 1/6$, total error $\epsilon = 6\epsilon_{\mathrm{PP},E} + 2\Gamma$, and leakage rate $\Gamma = 6\Gamma_{\mathrm{PP},0}$. High magnetic field prevents spin flips, restricting evolution to the three-dimensional $m = \pm 1/2$ subspaces, giving a survival probability asymptotic value of $A = 1/3$ and a leakage rate from collinear magnetic noise alone. Our NZ1 experiments, however, are not in the high-field regime. At low magnetic field and for short pulse periods, i.e., small Larmor phase $2\pi\nu_0\tau \ll 1$ corresponding to the left part of Fig. 4(a), $\Gamma_{\mathrm{PP},+} + \Gamma_{\mathrm{PP},-} = 2\Gamma_{\mathrm{PP},0}$ so $q_2 = q_1 = 36\Gamma_{\mathrm{PP},0}$, and again the theoretical expressions for y_0 and y_1 match our ansatz equation (C1) with $A = 1/4, B = 1/2, C = 1/4$, total error $\epsilon = 6\epsilon_{\mathrm{PP},E} + 2\Gamma$, and leakage rate $\Gamma = 3 \times 6\Gamma_{\mathrm{PP},0}$. In the low-field limit, both $m = \pm 1/2$ and $m = \pm 3/2$ leaked states are accessible, giving a survival probability asymptotic value of $A = 1/4$. Without a large external field, all three independent and identically distributed magnetic noise components contribute equally to the leakage rate.

When $\nu_0\tau$ approaches an antinode of $\mathcal{F}_{\mathcal{M}}^{\mathcal{I},\mathcal{E},\mathcal{L}}(\nu)$, the sideband terms become pronounced, and lead to a "Larmor resonance" peak as evident in Fig. 4. Physically, this corresponds to a combination of the precessing electron spins and our NZ1 pulse sequence in the presence of nonparallel magnetic gradient fields together inducing electron spin flips, which ultimately populate the $m = \pm 3/2$ leakage states. In this case our ansatz equation (C1) is insufficient, as $y_0 + y_1$ would be a double exponential, since the $m = \pm 1/2$ and $m = \pm 3/2$ leakage events occur at different rates. Such a double exponential in $(y_0 + y_1)/2$ would be difficult to decompose from curve-fitting alone, and so we accept that in the region of the Larmor resonance peak, the measured leakage rate is some kind of mixture of the $\Gamma_{\mathrm{PP},0}$ and $\Gamma_{\mathrm{PP},\pm}$ terms resulting from fitting to a single-exponential decay.

Figure 5 shows the fitting procedure to generate the data point in Fig. 4(a) with $t_{\mathrm{idle}} = 85$ ns. Like the data presented in Fig. 3, in Fig. 5(a) we plot the $|0\rangle$ return probability for both the standard NZ1y sequence (y_0) and the NZ1y sequence with the appended X gate (y_1). We then calculate the difference and sum curves, plotted in Fig. 5(b), and we fit them to separate exponential decay curves. We fit

$$y_0 - y_1 = 2B(1-p)^M, \tag{C7}$$
$$(y_0 + y_1)/2 = A + C(1-q)^M \tag{C8}$$

and extract $\epsilon_{\mathrm{PP}} = 6.65 \times 10^{-5}$ and $\Gamma_{\mathrm{PP}} = 1.06 \times 10^{-5}$ using Eqs. (C2) and (C3).

Since the leakage rate for small t_{idle} can be several orders of magnitude smaller than the total error, the accuracy of the leakage fit is limited by the range of $r = 3M$ in the experiments. For data shown in Fig. 4(a), the error in the fit becomes greater than or equal to the fit value for $t_{\mathrm{idle}} \leq 40$ ns and at $t_{\mathrm{idle}} = 60$ ns.

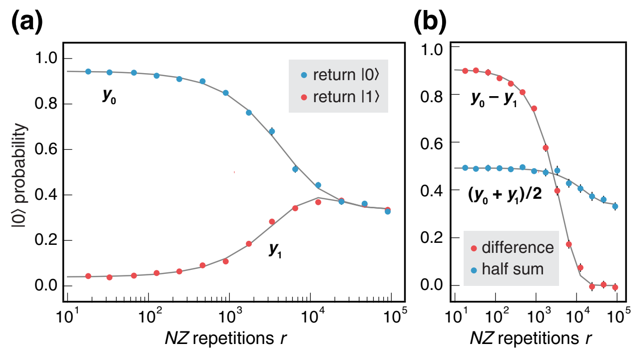

FIG. 5. NZ1y example dataset from Fig. 4(a), where $t_{\text{idle}} = 85$ ns. (a) The return probabilities for sequences with expected return to $|0\rangle$ are in blue and labeled y_0. The red points labeled y_1 are sequences that are expected to return $|1\rangle$. (b) The calculated $y_0 - y_1$ (red) and $(y_0 + y_1)/2$ (blue) curves are fitted to separate exponential decay curves (gray) to extract the error and leakage parameters. The fit gives $\epsilon_{\text{PP}} = 6.65 \times 10^{-5}$ and $\Gamma_{\text{PP}} = 1.06 \times 10^{-5}$. For this dataset, $T_2 = 714$ µs.

APPENDIX D: APPROXIMATE EXPRESSIONS FOR ERROR RATES

Asymptotic expressions for the total error rate ϵ_{PP} and the leakage error rate Γ_{PP} are given by

$$\epsilon_{\text{PP}} = \lim_{M\to\infty} \frac{1}{6M} \left(\int_0^\infty d\nu\, S_B(\nu) \times \mathcal{F}^{\mathcal{I}}_{\mathcal{M}}(\theta, \phi, \nu, M, f\tau, (1-f)\tau) + \int_0^\infty d\nu\, S_E(\nu) \mathcal{F}^{\mathcal{I}}_{E}(\theta, \phi, \nu, M, f\tau, (1-f)\tau) \right), \tag{D1}$$

$$\Gamma_{\text{PP}} = \lim_{M\to\infty} \frac{1}{6M} \int_0^\infty d\nu\, S_B(\nu) \times \mathcal{F}^{\mathcal{L}}_{\mathcal{M}}(\theta, \phi, \nu, M, f\tau, (1-f)\tau), \tag{D2}$$

where the leakage error magnetic filter function is $\mathcal{F}^{\mathcal{L}}_{\mathcal{M}} = \mathcal{F}^{\mathcal{I}}_{\mathcal{M}} - \mathcal{F}^{\mathcal{E}}_{\mathcal{M}}$ and $6M$ is the number of pulses in M repetitions of the basic NZ1 sequence. In this appendix, we determine analytic approximations to the integrals in the above error rate expressions.

For ease of analysis, we assume that the magnetic noise and exchange noise PSDs take the form

$$S(\nu) = \begin{cases} A, & 0 \le \nu < \nu_L, \\ A\dfrac{\nu_L}{\nu}, & \nu_L \le \nu < \nu_H, \\ A\dfrac{\nu_L \nu_H}{\nu^2}, & \nu_H \le \nu, \end{cases} \tag{D3}$$

where A sets the PSD size, ν_L is a low-frequency cutoff, and ν_H is a high-frequency cutoff. The PSD has a constant region at low frequency, a $1/f$ region, and a $1/f^2$ region. For comparison with experiment, we take for both magnetic noise and exchange noise $\nu_L = 0.1$ Hz, while for magnetic noise $\nu_{H,B} = 10$ kHz and for exchange noise $\nu_{H,E} = 1$ GHz. The PSD size parameters A_B and A_E are constrained by the frequency cutoffs and the values of T_2^* in the free-induction decay (FID) experiment and the number of oscillations N_{osc} in the Rabi experiment [18]. To relate T_2^* and A_B, we perform the filter function analysis for a single idle interval of increasing duration t for a two-electron state initialized and measured in a singlet state. The evolution due to magnetic noise in the collinear limit is integrable and yields the standard FID filter function of $\mathcal{F}_{\text{FID}}(\nu, t) = \sin^2(\pi\nu t)/(2\pi^2\nu^2)$. The collinear or high-field limit is sufficiently accurate for the FID experiment but is insufficient for NZ1 experiments. Evaluation of the frequency integral of the FID filter function against the magnetic noise PSD of Eq. (D3) gives the relation

$$A_B = \frac{1}{T_2^{*2}\nu_L\left(2 + \ln\frac{\nu_{H,B}}{\nu_L}\right)}. \tag{D4}$$

Similarly, to relate N_{osc} and A_E, we perform the filter function analysis for a single N rotation of increasing duration t for a DFS state initialized and measured in the $|0\rangle$ state. Up to a constant factor, the filter function for the Rabi experiment is the same as the FID filter function. In the small-ν_L and large-$\nu_{H,E}$ limit, the resulting relation between A_E and N_{osc} is

$$A_E = \frac{1}{N_{\text{osc}}^2 \nu_L t_{\text{pulse}}^2 \left(5 - 2\gamma - 2\ln 4\pi N_{\text{osc}}\nu_L t_{\text{pulse}}\right)}, \tag{D5}$$

where γ is Euler's constant.

We now perform the NZ1 frequency integrations for the exchange and nonsideband parts of the magnetic noise, whose filter functions take the form

$$\mathcal{F}(\nu, M) = \mathcal{F}(\nu, M=1)\frac{\sin^2(6M\pi\nu\tau)}{\sin^2(6\pi\nu\tau)} \tag{D6}$$

(momentarily suppressing additional parameters in the filter function arguments). In the limit of large M, the ratio of squared sines is a series of peaks located at $\nu_n = n/6\tau$, $n \in \mathbb{Z}$, of height M^2 and effective width $1/(6M\tau)$. The effect of this term in the frequency integral can then be approximated by a sum of δ functions:

$$\frac{\sin^2(6M\pi\nu\tau)}{\sin^2(6\pi\nu\tau)} \approx \frac{M}{6\tau}\sum_{n=-\infty}^{\infty} \delta(\nu - \nu_n). \tag{D7}$$

Specializing to NZ1y, we find that the exchange noise contribution to the error rate $\epsilon_{\mathrm{PP},E}$ is given by

$$\begin{aligned}\epsilon_{\mathrm{PP},E} &= \lim_{M\to\infty}\frac{1}{6M}\int_0^\infty d\nu\ S_E(\nu)\mathcal{F}_E^{\mathcal{I}}(\pi/2,\pi/2,\nu,M,f\tau,(1-f)\tau)\\ &\approx \frac{1}{6M}\frac{M}{6\tau}\sum_{n=1}^{\infty}S_E(\nu_n)\frac{2[2+\cos(4\pi\nu_n\tau)]\sin^2(\pi\nu_n f\tau)\sin^2(2\pi\nu_n\tau)}{\pi^2\nu_n^2},\end{aligned} \tag{D8}$$

where we have made the δ-function substitution and restricted the sum to positive frequency values. (By design, the zero-frequency contribution at $n=0$ is zero since the decoupling sequence and resultant filter function remove static noise.) The pulse periods τ of experimental interest are in the 10–1000-ns range, so all $\nu_n > \nu_L$; the sum samples the exchange noise PSD only in the $1/f$ and $1/f^2$ regions. Making the additional approximation that $\nu_{H,E}\to\infty$ (so that the $1/f$ region of the exchange noise PSD is extended to infinity), performing the sum, and keeping only the lowest order term in fractional pulse width f, we obtain

$$\begin{aligned}\epsilon_{\mathrm{PP},E} &\approx \frac{A_E f^2\nu_L\tau^2\,(3+\ln 27-2\ln(f\pi))}{8}.\\ &= \frac{3+\ln 27-2\ln \pi t_{\mathrm{pulse}}/(t_{\mathrm{idle}}+t_{\mathrm{pulse}})}{8N_{\mathrm{osc}}^2\left(5-2\gamma-2\ln 4\pi N_{\mathrm{osc}}\nu_L t_{\mathrm{pulse}}\right)}.\end{aligned} \tag{D9}$$

For parameters in our experiments, these approximations introduce relative errors in the exchange error rate of less than 1%.

For NZ1y magnetic error rate computations, we take the fractional pulse width $f=0$ approximation immediately (this cannot be done in the exchange error rate computation as the $f=0$ limit gives zero exchange noise). In this limit, the magnetic leakage and encoded error filter functions are identical, and the magnetic infidelity filter function is twice the leakage filter function. The asymptotic leakage error rate due to the nonsideband term $\Gamma_{\mathrm{PP},0}$ is then

$$\begin{aligned}\Gamma_{\mathrm{PP},0} &\approx \lim_{M\to\infty}\frac{1}{6M}\int_0^\infty d\nu S_B(\nu)\mathcal{F}_{\mathcal{M},0}^{\mathcal{L}}(\pi/2,\pi/2,\nu,M,0,\tau)\\ &= \lim_{M\to\infty}\frac{1}{6M}\int_0^\infty d\nu S_B(\nu)\frac{32(2+\cos 4\pi\nu\tau)\cos^2(\pi\nu\tau)\sin^4(\pi\nu\tau)}{3\pi^2\nu^2}\frac{\sin^2(6M\pi\nu\tau)}{\sin^2(6\pi\nu\tau)},\end{aligned} \tag{D10}$$

where $\mathcal{F}_{\mathcal{M},0}^{\mathcal{L}}$ is the magnetic leakage filter function without sideband terms. Using the same large-M δ-function approximation as in the exchange noise case and noting that $\nu_n > \nu_{H,B}$ for all n so that the sum samples the magnetic noise PSD only in the $1/f^2$ region, we obtain

$$\begin{aligned}\Gamma_{\mathrm{PP},0} &\approx \frac{1}{36\tau}\sum_{n=1}^{\infty}\frac{A_B\nu_L\nu_{H,B}}{\nu_n^2}\frac{32[2+\cos(4\pi\nu_n\tau)]\cos^2(\pi\nu_n\tau)\sin^4(\pi\nu_n\tau)}{3\pi^2\nu_n^2}\\ &= \frac{1}{3}A_B\pi^2\nu_L\nu_{H,B}\tau^3.\end{aligned} \tag{D11}$$

The sideband parts of the magnetic filter functions take the form

$$\mathcal{F}(\nu\pm\nu_0,M) = \mathcal{F}(\nu\pm\nu_0,M=1)\frac{\sin^2[6M\pi(\nu\pm\nu_0)\tau]}{\sin^2[6\pi(\nu\pm\nu_0)\tau]}, \tag{D12}$$

with ν_0 the electron Larmor frequency. In the large-M limit, the sidebands' δ-function peaks are shifted by the Larmor frequency $\pm\nu_0$. Notice that the shifting of the δ-function peaks has the effect of "unshifting" the $M = 1$ part of the sideband filter functions, so Larmor shifts appear only in the sampling of the noise PSD. The asymptotic leakage error rate contribution from the sidebands is then given by

$$\Gamma_{\mathrm{PP},+} + \Gamma_{\mathrm{PP},-} \approx \lim_{M\to\infty} \frac{1}{6M} \int_0^\infty d\nu S_B(\nu) \left(\mathcal{F}^{\mathcal{L}}_{\mathcal{M},0}(\pi/2, \pi/2, \nu + \nu_0, M, 0, \tau) + \mathcal{F}^{\mathcal{L}}_{\mathcal{M},0}(\pi/2, \pi/2, \nu - \nu_0, M, 0, \tau)\right)$$
$$\approx \frac{1}{36\tau} \sum_{n=-\infty}^{\infty} \frac{A_B \nu_L \nu_{H,B}}{(\nu_n - \nu_0)^2} \frac{32[2 + \cos(4\pi\nu_n\tau)] \cos^2(\pi\nu_n\tau) \sin^4(\pi\nu_n\tau)}{3\pi^2\nu_n^2}, \tag{D13}$$

where we have again sampled the magnetic noise PSD only in the $1/f^2$ region. (This is incorrect very near resonance, when $|\nu_n - \nu_0| = |n/6\tau - \nu_0| < \nu_{H,B}$, since the δ functions begin to sample the PSD in the $1/f$ and constant regions. For the first resonance $n = 1$, with $B_0 = 50$ μT and $\nu_{H,B} = 10$ kHz, this occurs when the pulse period τ is within 270 ps of the resonance at $\tau_R = 119.080$ ns, at which point the lowest-order perturbative filter function theory is already inaccurate.)

Performing the sum in Eq. (D13), combining the sideband and nonsideband contributions, and substituting for the magnetic noise PSD amplitude A_B from Eq. (D4), we obtain an approximate per-pulse leakage error rate

$$\Gamma_{\mathrm{PP}} = \Gamma_{\mathrm{PP},0} + \Gamma_{\mathrm{PP},+} + \Gamma_{\mathrm{PP},-}, \tag{D14}$$

$$\Gamma_{\mathrm{PP},0} \approx \frac{\pi^2 \nu_{H,B} \tau^3}{3T_2^{*2}\left(2 + \ln\frac{\nu_{H,B}}{\nu_L}\right)}, \tag{D15}$$

$$\Gamma_{\mathrm{PP},+} + \Gamma_{\mathrm{PP},-} \approx \Gamma_{\mathrm{PP},0} \left(\frac{4\left(-4\sin 2\theta_\ell + 2\sin 3\theta_\ell - 4\sin 4\theta_\ell + \theta_\ell\left(11 - 4\cos\theta_\ell + 8\cos 2\theta_\ell + \cos 3\theta_\ell + 2\cos 4\theta_\ell\right)\right)}{\theta_\ell^3\left(1 + 2\cos 2\theta_\ell\right)^2}\right). \tag{D16}$$

The effect of the sidebands relative to the nonsideband leakage is determined completely by $\theta_\ell \equiv 2\pi\nu_0\tau$, the accumulated Larmor phase in a pulse period. Compared with direct numerical integration of Eq. (D2) at $M = 10^4$, the approximate leakage error rate expression has a mean relative error of 5% across the experimental t_{idle} sweep, over which the leakage error rate increases by 4 orders of magnitude. The approximate per-pulse total error rate is given by

$$\epsilon_{\mathrm{PP}} \approx \epsilon_{\mathrm{PP},E} + 2\Gamma_{\mathrm{PP}}. \tag{D17}$$

The leakage error rate equations (D14)–(D16) and total error rate equations (D9) and (D14)–(D17) are plotted in Fig. 4 with $T_2^* = 2$ μs, $N_{\mathrm{osc}} = 25$, $\nu_L = 0.1$ Hz, $\nu_{H,B} = 10$ kHz, $B_0 = 50$ μT, $\nu_0 = 1.4$ MHz, $t_{\mathrm{pulse}} = 10$ ns, differing t_{idle}, and $\tau = t_{\mathrm{pulse}} + t_{\mathrm{idle}}$. For these parameter values, the leakage error rate sideband contributions always dominate the nonsideband contributions, ranging from 2 times at $t_{\mathrm{idle}} = 10$ ns to 143 times at $t_{\mathrm{idle}} = 100$ ns as t_{idle} approaches the first Larmor resonance.

APPENDIX E: MONTE CARLO SIMULATIONS

Numerical simulations of noise qubit dynamics during pulse sequences use a simple eight-dimensional complex vector for the three-spin DFS qubits, implemented with an in-house code written in C++ and PYTHON entitled "Python Quantum Exchange Simulation Toolsuite" (pyQUEST). These three spins experience a piecewise constant Hamiltonian including only pairwise interactions consisting of exchange operations and noisy magnetic fields. For all simulations here, these noisy magnetic fields are represented by identical, independent distributions for each vector component interacting with each of the three spins. The distribution used is Gaussian noise with a $1/f$ power spectral density. Charge noise is simulated similarly to magnetic noise, with identical, independent distributions for fluctuating miscalibration of both exchange pairs. Hence, each simulation uses 11 independent $1/f$ variables in total: nine for three-dimensional magnetic fields on each of three quantum dots, plus charge noise on each of two exchange axes.

To simulate $1/f$ noise, we use a modified version of the Voss-McCartney algorithm [44] wherein we take the sum of multiple random numbers, updated at different frequencies, to get an overall $1/f$ spectrum. Specifically, each noise variable is the sum of 100 Gaussian random fluctuators, with update frequencies logarithmically spaced between the low-frequency and high-frequency cutoffs. The PSD for such a variable goes as $1/f$ between its cutoffs, and rolls over to white at lower frequencies or $1/f^2$ at higher frequencies. Each fluctuator also gets a random phase offset to desynchronize their updates and produce a smoother spectrum. When sampling our noise variables, we sample their integrated value over some finite time window, so we need compute only one sample per simulated pulse or idle. Since the sum of multiple Gaussian variables is itself a Gaussian variable, this can always be done efficiently and exactly, even for time steps much longer than the inverse update frequency.

Empirically, we find that charge noise tends to have a $1/f$ dependence over the full, experimentally accessible range of frequencies, so for our simulation noise generators, we set its high-frequency cutoff to more than 1 GHz. Magnetic noise results from relatively slow, nuclear processes, and so we set its high-frequency cutoff to 10 kHz. Neither high-frequency cutoff is known exactly (or possibly even physically meaningfully); however, simulations of the present experiments are insensitive to this number when it is set to a reasonable value, and when the total noise power is calibrated to replicate decays for free-evolution and triple-quantum-dot experiments as described in the main text.

For each value of external magnetic field and t_{idle} in Fig. 4, we simulate a full NZ1y experiment, except that instead of an ensemble of single-shot measurements, we take the singlet probability directly from the numerical spin-state vector and advance the simulator clock (relevant to $1/f$ noise generators) so as to account for the time those single-shot measurements consume. The duration of piecewise constant intervals in our simulation is set by events, i.e., by pulses (intervals of time t_{pulse}) and idles (intervals of time t_{idle}). Since the Larmor evolution and the high-frequency noise cutoffs are so slow relative to pulsing speeds, entire pulses and idle times can be collapsed into single constant-evolution segments with use of the averaged integrated noise over that segment; additional time segmentation adds a negligible difference in accuracy. For $t_{\mathrm{idle}} < 100$ ns, we average each NZ experiment (at repetition number r) 250 times, and then sweep r, maintaining continuity of the $1/f$ noise generation across repetitions. For $t_{\mathrm{idle}} \geq 100$ ns, we reduce the averaging to 100 instances. More averaging is required at smaller t_{idle} since the leakage rate is so small. The simulated experiment is then fit with use of the same procedure as described in Appendix C.

[1] L. Viola and S. Lloyd, Dynamical suppression of decoherence in two-state quantum systems, Phys. Rev. A **58**, 2733 (1998).

[2] N. Ezzell, B. Pokharel, L. Tewala, G. Quiroz, and D. A. Lidar, Dynamical decoupling for superconducting qubits: A performance survey, Phys. Rev. Appl. **20**, 064027 (2023).

[3] A. M. Tyryshkin, S. Tojo, J. J. L. Morton, H. Riemann, N. V. Abrosimov, P. Becker, H.-J. Pohl, T. Schenkel, M. L. W. Thewalt, K. M. Itoh, and S. A. Lyon, Electron spin coherence exceeding seconds in high-purity silicon, Nat. Mater. **11**, 143 (2012).

[4] M. Veldhorst, J. C. C. Hwang, C. H. Yang, A. W. Leenstra, B. de Ronde, J. P. Dehollain, J. T. Muhonen, F. E. Hudson, K. M. Itoh, A. Morello, and A. S. Dzurak, An addressable quantum dot qubit with fault-tolerant control-fidelity, Nat. Nanotechnol. **9**, 981 (2014).

[5] K. Saeedi, S. Simmons, J. Z. Salvail, P. Dluhy, H. Riemann, N. V. Abrosimov, P. Becker, H.-J. Pohl, J. J. L. Morton, and M. L. W. Thewalt, Room-temperature quantum bit storage exceeding 39 minutes using ionized donors in silicon-28, Science **342**, 830 (2013).

[6] J. T. Muhonen, J. P. Dehollain, A. Laucht, F. E. Hudson, R. Kalra, T. Sekiguchi, K. M. Itoh, D. N. Jamieson, J. C. McCallum, A. S. Dzurak, and A. Morello, Storing quantum information for 30 seconds in a nanoelectronic device, Nat. Nanotechnol. **9**, 986 (2014).

[7] J. Bylander, S. Gustavsson, F. Yan, F. Yoshihara, K. Harrabi, G. Fitch, D. G. Cory, Y. Nakamura, J.-S. Tsai, and W. D. Oliver, Noise spectroscopy through dynamical decoupling with a superconducting flux qubit, Nat. Phys. **7**, 565 (2011).

[8] G. A. Álvarez and D. Suter, Measuring the spectrum of colored noise by dynamical decoupling, Phys. Rev. Lett. **107**, 230501 (2011).

[9] J. Kerckhoff, B. Sun, B. Fong, C. Jones, A. Kiselev, D. Barnes, R. Noah, E. Acuna, M. Akmal, S. Ha, J. Wright, B. Thomas, C. Jackson, L. Edge, K. Eng, R. Ross, and T. Ladd, Magnetic gradient fluctuations from quadrupolar ^{73}Ge in Si/SiGe exchange-only qubits, PRX Quantum **2**, 010347 (2021).

[10] E. Kawakami, T. Jullien, P. Scarlino, D. R. Ward, D. E. Savage, M. G. Lagally, V. V. Dobrovitski, M. Friesen, S. N. Coppersmith, M. A. Eriksson, and L. M. K. Vandersypen, Gate fidelity and coherence of an electron spin in an Si/SiGe quantum dot with micromagnet, Proc. Natl. Acad. Sci. **113**, 11738 (2016).

[11] J. Yoneda, K. Takeda, T. Otsuka, T. Nakajima, M. R. Delbecq, G. Allison, T. Honda, T. Kodera, S. Oda, Y. Hoshi,

N. Usami, K. M. Itoh, and S. Tarucha, A quantum-dot spin qubit with coherence limited by charge noise and fidelity higher than 99.9%, Nat. Nanotechnol. **13**, 102 (2018).

[12] T. Struck, A. Hollmann, F. Schauer, O. Fedorets, A. Schmidbauer, K. Sawano, H. Riemann, N. V. Abrosimov, Ł. Cywiński, D. Bougeard, and L. R. Schreiber, Low-frequency spin qubit energy splitting noise in highly purified ^{28}Si/SiGe, npj Quantum Inf. **6**, 1 (2020).

[13] T. Nakajima, A. Noiri, K. Kawasaki, J. Yoneda, P. Stano, S. Amaha, T. Otsuka, K. Takeda, M. R. Delbecq, G. Allison, A. Ludwig, A. D. Wieck, D. Loss, and S. Tarucha, Coherence of a driven electron spin qubit actively decoupled from quasistatic noise, Phys. Rev. X **10**, 011060 (2020).

[14] E. J. Connors, J. J. Nelson, and J. M. Nichol, Charge-noise spectroscopy of Si/SiGe quantum dots via dynamically-decoupled exchange oscillations, Nat. Commun. **13**, 940 (2022).

[15] E. L. Hahn, Spin echoes, Phys. Rev. **80**, 580 (1950).

[16] E. Knill, R. Laflamme, and L. Viola, Theory of quantum error correction for general noise, Phys. Rev. Lett. **84**, 2525 (2000).

[17] D. P. DiVincenzo, D. Bacon, J. Kempe, G. Burkard, and K. B. Whaley, Universal quantum computation with the exchange interaction, Nature **408**, 339 (2000).

[18] R. W. Andrews, C. Jones, M. D. Reed, A. M. Jones, S. D. Ha, M. P. Jura, J. Kerckhoff, M. Levendorf, S. Meenehan, S. T. Merkel, A. Smith, B. Sun, A. J. Weinstein, M. T. Rakher, T. D. Ladd, and M. G. Borselli, Quantifying error and leakage in an encoded Si/SiGe triple-dot qubit, Nat. Nanotechnol. **14**, 747 (2019).

[19] L.-A. Wu and D. A. Lidar, Creating decoherence-free subspaces using strong and fast pulses, Phys. Rev. Lett. **88**, 207902 (2002).

[20] J. R. West and B. H. Fong, Exchange-only dynamical decoupling in the three-qubit decoherence free subsystem, New J. Phys. **14**, 083002 (2012).

[21] P.-A. Mortemousque, B. Jadot, E. Chanrion, V. Thiney, C. Bäuerle, A. Ludwig, A. D. Wieck, M. Urdampilleta, and T. Meunier, Enhanced spin coherence while displacing electron in a two-dimensional array of quantum dots, PRX Quantum **2**, 030331 (2021).

[22] B. H. Fong and S. M. Wandzura, Universal quantum computation and leakage reduction in the 3-qubit decoherence free subsystem, Quantum Inf. Comput. **11**, 1003 (2011).

[23] B. M. Maune, M. G. Borselli, B. Huang, T. D. Ladd, P. W. Deelman, K. S. Holabird, A. A. Kiselev, I. Alvarado-Rodriguez, R. S. Ross, A. E. Schmitz, M. Sokolich, C. A. Watson, M. F. Gyure, and A. T. Hunter, Coherent singlet-triplet oscillations in a silicon-based double quantum dot, Nature **481**, 344 (2012).

[24] K. Eng, T. D. Ladd, A. Smith, M. G. Borselli, A. A. Kiselev, B. H. Fong, K. S. Holabird, T. M. Hazard, B. Huang, P. W. Deelman, I. Milosavljevic, A. E. Schmitz, R. S. Ross, M. F. Gyure, and A. T. Hunter, Isotopically enhanced triple-quantum-dot qubit, Sci. Adv. **1**, e1500214 (2015).

[25] M. D. Reed, B. M. Maune, R. W. Andrews, M. G. Borselli, K. Eng, M. P. Jura, A. A. Kiselev, T. D. Ladd, S. T. Merkel, I. Milosavljevic, E. J. Pritchett, M. T. Rakher, R. S. Ross, A. E. Schmitz, A. Smith, J. A. Wright, M. F. Gyure, and A. T. Hunter, Reduced sensitivity to charge noise in semiconductor spin qubits via symmetric operation, Phys. Rev. Lett. **116**, 110402 (2016).

[26] C. Jones, M. A. Fogarty, A. Morello, M. F. Gyure, A. S. Dzurak, and T. D. Ladd, Logical qubit in a linear array of semiconductor quantum dots, Phys. Rev. X **8**, 021058 (2018).

[27] M. G. Borselli, K. Eng, R. S. Ross, T. M. Hazard, K. S. Holabird, B. Huang, A. A. Kiselev, P. W. Deelman, L. D. Warren, I Milosavljevic, A. E. Schmitz, M. Sokolich, M. F. Gyure, and A. T. Hunter, Undoped accumulation-mode Si/SiGe quantum dots, Nanotechnology **26**, 375202 (2015).

[28] A. Jones, E. Pritchett, E. Chen, T. Keating, R. Andrews, J. Blumoff, L. De Lorenzo, K. Eng, S. Ha, A. Kiselev, S. Meenehan, S. Merkel, J. Wright, L. Edge, R. Ross, M. Rakher, M. Borselli, and A. Hunter, Spin-blockade spectroscopy of Si/Si-Ge quantum dots, Phys. Rev. Appl. **12**, 014026 (2019).

[29] W. Ha, S. D. Ha, M. D. Choi, Y. Tang, A. E. Schmitz, M. P. Levendorf, K. Lee, J. M. Chappell, T. S. Adams, D. R. Hulbert, E. Acuna, R. S. Noah, J. W. Matten, M. P. Jura, J. A. Wright, M. T. Rakher, and M. G. Borselli, A flexible design platform for Si/Si-Ge exchange-only qubits with low disorder, Nano Lett. **22**, 1443 (2022).

[30] D. M. Zajac, T. M. Hazard, X. Mi, K. Wang, and J. R. Petta, A reconfigurable gate architecture for Si/SiGe quantum dots, Appl. Phys. Lett. **106**, 223507 (2015).

[31] J. Z. Blumoff, *et al.*, Fast and high-fidelity state preparation and measurement in triple-quantum-dot spin qubits, PRX Quantum **3**, 010352 (2022).

[32] G. Burkard, T. D. Ladd, A. Pan, J. M. Nichol, and J. R. Petta, Semiconductor spin qubits, Rev. Mod. Phys. **95**, 025003 (2023).

[33] H. Y. Carr and E. M. Purcell, Effects of diffusion on free precession in nuclear magnetic resonance experiments, Phys. Rev. **94**, 630 (1954).

[34] S. Meiboom and D. Gill, Modified spin-echo method for measuring nuclear relaxation times, Rev. Sci. Instrum. **29**, 688 (1958).

[35] M. T. Madzik, T. D. Ladd, F. E. Hudson, K. M. Itoh, A. M. Jakob, B. C. Johnson, J. C. McCallum, D. N. Jamieson, A. S. Dzurak, A. Laucht, and A. Morello, Controllable freezing of the nuclear spin bath in a single-atom spin qubit, Sci. Adv. **6**, eaba3442 (2020).

[36] F. K. Malinowski, F. Martins, P. D. Nissen, E. Barnes, Ł. Cywiński, M. S. Rudner, S. Fallahi, G. C. Gardner, M. J. Manfra, C. M. Marcus, and F. Kuemmeth, Notch filtering the nuclear environment of a spin qubit, Nat. Nanotechnol. **12**, 16 (2017).

[37] H. Bluhm, S. Foletti, I. Neder, M. Rudner, D. Mahalu, V. Umansky, and A. Yacoby, Dephasing time of GaAs electron-spin qubits coupled to a nuclear bath exceeding 200 μs, Nat. Phys. **7**, 109 (2011).

[38] A. J. Weinstein, *et al.*, Universal logic with encoded spin qubits in silicon, Nature **615**, 817 (2023).

[39] F. Setiawan, H.-Y. Hui, J. P. Kestner, X. Wang, and S. D. Sarma, Robust two-qubit gates for exchange-coupled qubits, Phys. Rev. B **89**, 085314 (2014).

[40] T. L. Brecht, Bulletin of the APS March Meeting 2023, Abstract Z74.00002.

[41] G. Quiroz, B. Pokharel, J. Boen, L. Tewala, V. Tripathi, D. Williams, L.-A. Wu, P. Titum, K. Schultz, and D. Lidar,

Dynamically generated decoherence-free subspaces and subsystems on superconducting qubits, arXiv:2402.07278.

[42] L. Viola and E. Knill, Robust dynamical decoupling of quantum systems with bounded controls, Phys. Rev. Lett. **90**, 037901 (2003).

[43] M. Cai and K. Xia, Optimizing continuous dynamical decoupling with machine learning, Phys. Rev. A **106**, 042434 (2022).

[44] R. F. Voss and J. Clarke, "$1/f$ noise" in music: Music from $1/f$ noise, J. Acoust. Soc. Am. **63**, 258 (1978).